

1 **Tephrochronological constraints on the timing and nature of sea-level**  
2 **change prior to and during glacial termination V**

3 Biagio Giaccio<sup>1,2</sup>, Gianluca Marino<sup>3,4</sup>, Fabrizio Marra<sup>2\*</sup>, Lorenzo Monaco<sup>5</sup>, Alison Pereira  
4<sup>6,7</sup>, Giovanni Zanchetta<sup>8</sup>, Mario Gaeta<sup>5</sup>, Niklas Leicher<sup>9</sup>, Sébastien Nomade<sup>7</sup>, Danilo M.  
5 Palladino<sup>5</sup>, Gianluca Sottili<sup>5</sup>, Hervé Guillou<sup>7</sup>, Vincent Scao<sup>7</sup>

6

7 1 Istituto di Geologia Ambientale e Geoingegneria, CNR, Roma, Italy

8 2 Istituto Nazionale di Geofisica e Vulcanologia, Rome, Italy

9 3 Centro de Investigación Mariña, GEOMA, Palaeoclimatology Lab, Universidade de Vigo, Vigo, Spain

10 4 Research School of Earth Sciences, The Australian National University, Canberra, Australian Capital

11 Territory, Australia

12 5 Sapienza Università di Roma, Dipartimento di Scienze della Terra, Piazzale Aldo Moro 5, 00185, Roma, Italy

13 6 Département Hommes et environnements, Muséum national d'Histoire naturelle, UMR 7194 du CNRS, 1 rue

14 René Panhard, 75013 Paris, France.

15 7 Laboratoire des Sciences du Climat et de l'Environnement, LSCE/IPSL, CEA-CNRS-UVSQ, Université Paris-

16 Saclay, F-91191 Gif-sur-Yvette, France.

17 8 Dipartimento di Scienze della Terra, University of Pisa, Pisa, Italy

18 9 Institute of Geology and Mineralogy, University of Cologne, Cologne, Germany

19

20 \*corresponding author: [fabrizio.marra@ingv.it](mailto:fabrizio.marra@ingv.it)

21

22 **Keywords**

23 MIS 12 to MIS 11 transition; Aggradational successions; Meltwater pulse events; Heinrich-  
24 like events; Middle Pleistocene; <sup>40</sup>Ar/<sup>39</sup>Ar geochronology

25

26 **Abstract**

27 Glacial-interglacial variations in ice volume and sea level are essential components of the  
28 Pleistocene global climate evolution. Deciphering the timing of change of these key climate  
29 parameters with respect to the insolation forcing is central to understanding the processes

1 controlling glacial terminations. Here we exploit the sensitivity of the Paleo Tiber River  
2 (central Italy) to sea-level forced changes in the base level and the frequent occurrence of  
3 datable tephra layers in its sedimentary successions to reconstruct the timing of the relative  
4 sea-level (RSL) change between 450 and 403 ka, i.e., across the glacial termination (T-V) that  
5 marks the transition between Marine Isotope Stage (MIS) 12 and MIS 11. The analysis hinges  
6 on new stratigraphic data, tephra geochemical fingerprinting, and  $^{40}\text{Ar}/^{39}\text{Ar}$  dating from a  
7 fluvial section that represents the inland counterpart of the near mouth, coastal aggradational  
8 successions of the San Paolo Formation (SPF). Tephra correlation indicates that the morpho-  
9 stratigraphic record of the inland section is as sensitive to the sea-level change as its coastal  
10 counterparts, which makes it ideal to complement previous RSL reconstructions from the  
11 Tiber River catchment basin, thereby providing a more detailed picture of the sea-level  
12 history across T-V. Combined sedimentological and morphological proxies of the composed  
13 inland-coastal SPF record document the occurrence of two phases of relatively rapid sea-level  
14 rise, here interpreted as meltwater pulse (MWP) events. The earlier MWP occurred between  
15  $\sim 450$  and  $\sim 445$  ka and matches a relatively minor episode of the sea-level rise documented in  
16 an existing RSL record, while the younger MWP at  $\sim 430$  ka corresponds to the high  
17 amplitude sea-level rise that marks T-V. We find that both MWPs coincide with episodes of  
18 ice-rafted debris deposition in the North Atlantic (Heinrich-like events) and with attendant  
19 Southern Hemisphere warming, plausibly associated with the bipolar seesaw.  
20

21

## 22 **1. Introduction**

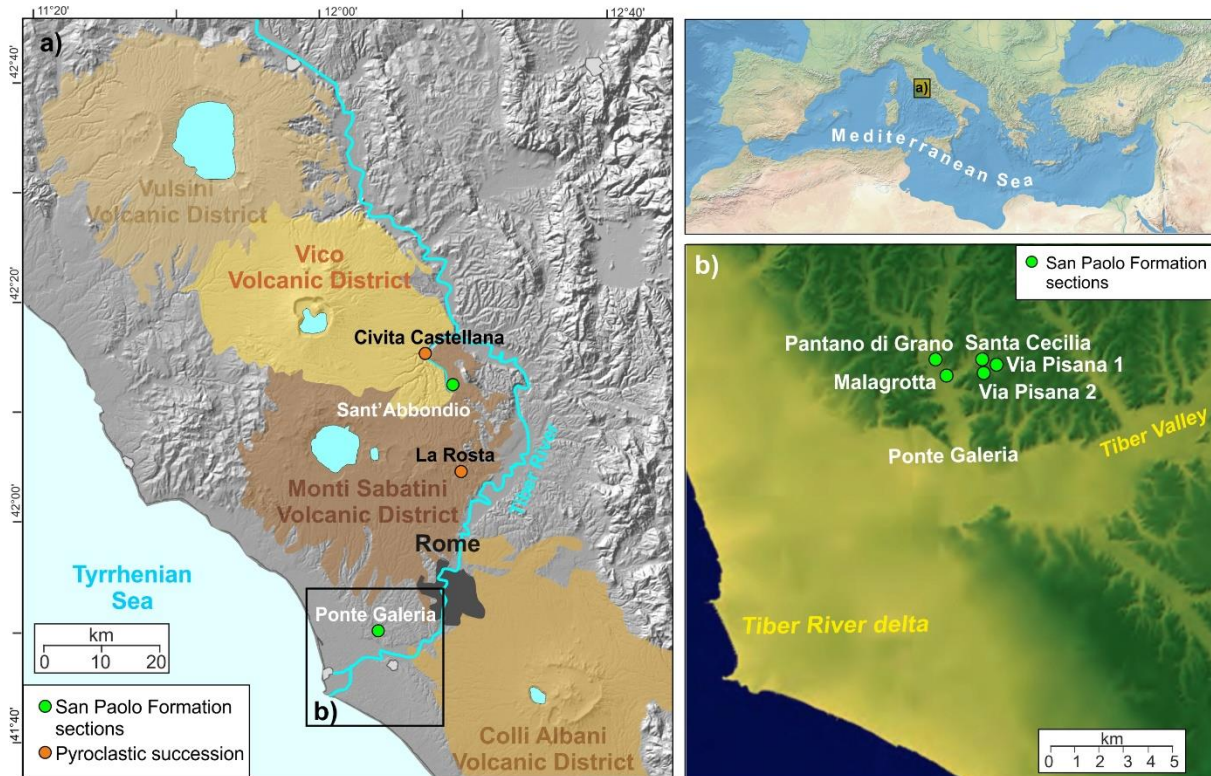
23 Glacial Marine Isotope Stage 12 (MIS 12) and the ensuing glacial termination (Termination  
24 V, T-V) that marks the transition into the long-lasting interglacial climate conditions of MIS  
25 11 represent a fundamental step in the evolution of the Pleistocene glacial-interglacial cycles  
26 (e.g., Droxler et al., 2003). The glacial maximum of MIS 12 constitutes the culmination of the  
27 stepwise intensification of glacial conditions (greater ice volume, lower atmospheric  $\text{CO}_2$   
28 concentrations) that accompanied the Middle Pleistocene Transition and the attendant  
29 emergence of the long, high-amplitude, and saw-tooth structured glacial-interglacial cycles  
30 (Elderfield et al., 2012; McClymont et al., 2013; Rohling et al., 2014; Chalk et al., 2017). The  
31 onset of MIS 11 coincided with the so-called “Mid-Brunhes Event”, during which glacial-  
32 interglacial cycles underwent a further increase in amplitude due to the development of more  
33 prominent interglacial conditions than in the lukewarm interglacial periods that occurred  
34 earlier (Jouzel et al., 2007; Lüthi et al., 2008; Barth et al., 2018; Ao et al., 2020). T-V featured  
35 the largest amplitude changes in ice volume (sea level) of the past millions of years (e.g.,

1 Droxler et al., 2003). The volume of the continental ice sheets during MIS 12 plausibly  
2 exceeded that of the last glacial maximum (Rohling et al., 1988), while extensive polar ice  
3 melting during MIS 11 (Blackburn et al., 2020) caused sea level to rise up to several meters  
4 above present levels (Raymo and Mitrovica, 2012; Dutton et al., 2015). These lines of  
5 evidence pose a serious challenge to the theory that ascribes Quaternary glaciations to orbital  
6 forcing (Milanković, 1941) and point to the potentially important role of climate feedbacks  
7 (Berger and Wefer, 2003) to explain the occurrence of the highest amplitude glacial  
8 termination at a time of comparatively small orbital forcing (e.g., Imbrie and Imbrie, 1980;  
9 Paillard, 2001). Changes in atmospheric CO<sub>2</sub> concentrations and continental ice volume (sea  
10 level) have been proposed as important climate feedbacks to explain the climate changes  
11 associated with the Middle to Late Pleistocene glacial-interglacial cycles (Chalk et al., 2017),  
12 given their impact on the radiative forcing of climate on 10<sup>2</sup>-10<sup>4</sup>-year timescales (Hansen et  
13 al., 2007, 2013; Rohling et al., 2018). Recent studies have provided detailed documentation of  
14 the atmospheric CO<sub>2</sub> changes around T-V (Nehrbass-Ahles et al., 2020), while the timing of  
15 the variations in global ice volume (sea level) and their relationships with orbital forcing  
16 around this key glacial-interglacial transition remain less well documented.

17 Discerning the different role played by orbital forcing and climate feedbacks and solving the  
18 above-mentioned open issues calls for precisely and independently (i.e., radioisotopically)  
19 dated records that can be compared with the insolation time-series that rely on the so-called  
20 “orbital solutions” (Laskar et al., 2004). A reliable chronological framework is available for  
21 the last glacial-interglacial cycle (e.g., Lambeck et al., 2014; Dutton and Lambeck, 2012),  
22 while the chronology of older ice-volume (sea-level) changes is generally based on the  
23 alignments of relative sea level (RSL) records to other well-dated paleoclimate time series  
24 (Rohling et al., 2009; Grant et al., 2014), and thus lack direct age control. This also affects our  
25 ability to decipher the so-called meltwater pulse events, relatively brief periods of rapid sea-  
26 level rise (e.g., Fairbanks et al., 1989; Deschamps et al., 2012) and meltwater release to the

1 polar oceans that impact ocean circulation and climate on regional to global scales (Denton et  
2 al., 2010; Weber et al., 2014; Marino et al., 2015; Rohling et al., 2019).

3



4

5 **Figure 1.** Reference maps of the study area. **a)** Shaded relief, digital elevation model (DEM)  
6 image of the lower portion of the hydrographic network of the Tiber River, within the domain  
7 of the Latium volcanic districts, showing the locations of the investigated San Paolo  
8 Formation (Sant'Abbondio) and of the pyroclastic succession (La Rosta sections). The  
9 location of previously investigated San Paolo Formation and pyroclastic sections are also  
10 shown. **b)** Details of the Ponte Galeria area with the location of the individual sections  
11 belonging to the San Paolo Formation.  
12

13 The so-called “aggradational successions” of the Paleo Tiber River, central Italy, represent a  
14 radioisotopically dated ( $^{14}\text{C}$  and  $^{40}\text{Ar}/^{39}\text{Ar}$ ) system of morpho-sedimentary units that formed in  
15 response to sea-level rise during the last eight glacial-interglacial transitions (Karner and  
16 Renne, 1998; Karner and Marra, 1998; Florindo et al., 2007; Marra et al., 2008, 2013, 2016a,  
17 2016b; Marra and Florindo, 2014; Luberti et al., 2017). This composite record can thus  
18 provide key radioisotopic chronological constraints that generally lack in the Middle  
19 Pleistocene sea-level records, and that thus can be used to better evaluate the relationship

1 between insolation changes and sea-level oscillations. We focus on the sedimentological  
2 features and geochronological constrains of new investigated sections of the San Paolo  
3 Formation (SPF, Fig. 1), belonging to the system of aggradational successions of the Paleo  
4 Tiber River, to refine the  $^{40}\text{Ar}/^{39}\text{Ar}$  chronology of the glacial-interglacial sea-level change  
5 between ~450 ka and ~400 ka. Specifically, we integrate recently reported  $^{40}\text{Ar}/^{39}\text{Ar}$  age  
6 determinations of the late stages of MIS 11c (Pereira et al., 2020) with new  $^{40}\text{Ar}/^{39}\text{Ar}$  dating  
7 and tephrochronological constraints through the late stages of the MIS 12. This dataset allows  
8 refining in unprecedented detail the timing of rapid (or even abrupt) ice-sheet melting during  
9 late MIS 12 and around T-V, i.e., the glacial-interglacial transition featuring the highest  
10 amplitude of change over the last millions of years (e.g., Droxler et al., 2003).

11  
12

## 13 **2. Background information and geological setting**

### 14 ***2.1. Tectonic and volcanological setting of the Tyrrhenian margin***

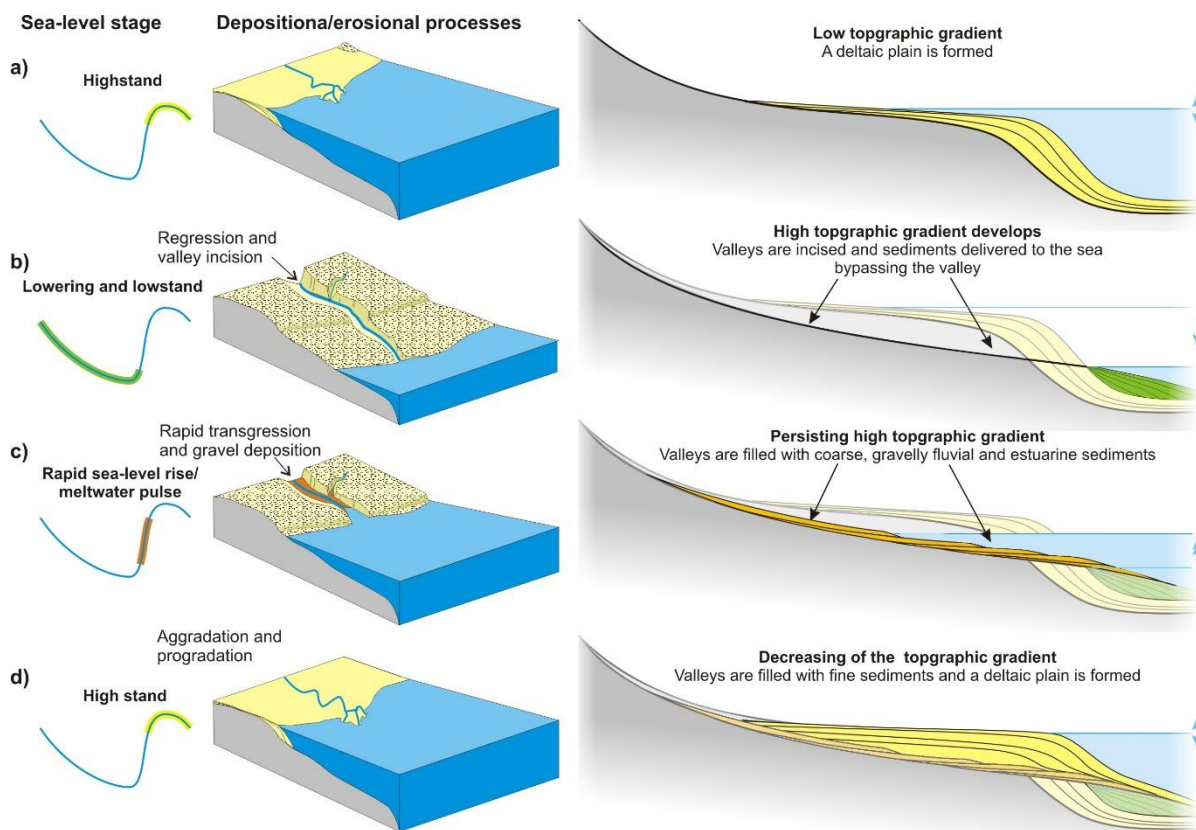
15 The Tyrrhenian Sea margin of central Italy, where the Tiber River and its valleys are located,  
16 developed as a back-arc basin since the Miocene (Malinverno and Ryan, 1986; Patacca et al.,  
17 1990), while the Paleo-Tiber delta formed southwest of Rome around 800 ka (Marra and  
18 Florindo, 2014). This region was subsequently affected by intense, explosive volcanic activity  
19 that formed the so-called “Roman Magmatic Region”, which was active during Middle to  
20 Late Pleistocene (Conticelli and Peccerillo, 1992). Two main uplift phases at ~800 ka and  
21 since ~250 ka have led to a progressive seaward migration of the coast (Marra et al., 2019a).  
22 Throughout this period, the sedimentary processes in the coastal and in the inland area were  
23 mainly controlled by the interaction between tectonic vertical movements and glacio-eustatic  
24 fluctuations (Luberti et al., 2017). Based on the comparison between the average uplift rate of  
25 the last 250 ka (0.24 mm/yr, Marra et al., 2019a) and the sedimentation rate during the  
26 aggradational phases (e.g., 2.3 mm/yr, Marra et al. (2019b) concluded that glacio-eustasy

1 overrides the tectonic effects, which only impact the accommodation space, and, in turn, the  
2 total thickness (rather than the timing of deposition) of each aggradational succession.

3  
4 **2.2. *The aggradational sedimentary successions of the Paleo Tiber River***

5 The hydrographic network of the Paleo Tiber River developed over a broad area that extends  
6 ~100 km north and south of the modern delta since the Late Pliocene-Early Pleistocene, in  
7 response to both regional uplift and glacioeustatic oscillations (e.g., Mancini et al., 2007) (Fig.  
8 2). The so-called “aggradational successions” that fill(ed) the valleys of the (Paleo) Tiber  
9 River have thicknesses of up to 70 m (Marra et al., 2008, 2013) and consist each of a basal  
10 unconformity surface upon which a fining-upward sequence of gravel, sand, silt, and clay  
11 deposited (Karner and Marra, 1998). Sedimentological and stratigraphic analyses of these  
12 successions, argon–argon ( $^{40}\text{Ar}/^{39}\text{Ar}$ ) and radiocarbon ( $^{14}\text{C}$ ) dating of the interspersed tephra  
13 and peat layers, and complementary paleomagnetic constraints collectively demonstrate the  
14 dominant control of the Pleistocene glacial-interglacial sea-level changes on their deposition  
15 (Karner and Renne, 1998; Karner and Marra, 1998; Florindo et al., 2007; Marra et al., 2008,  
16 2013, 2016a, 2016b; Marra and Florindo, 2014; Luberti et al., 2017). Specifically, shoreline  
17 retreat and sea-level lowering during glacial periods lead to the progressive incision of a basal  
18 erosional surface, while the fining-upward successions of clastic sediments that drape over  
19 these surfaces represent the sedimentary response of the Paleo Tiber River to sea-level rise at  
20 glacial terminations until highstand conditions are established (Fig. 2).

21



1  
2  
3  
4  
5  
6  
7  
8  
9  
10  
11  
12  
13  
14  
15  
16  
17  
18  
19  
20  
21  
22  
23  
24  
25  
26  
27  
28

**Figure 2.** Sketch explaining the mechanisms of formation of the Tiber River valley's aggradational succession in response to glacial-interglacial sea-level (continental ice-volume) change (cf. Karner and Renne, 1998; Karner and Marra, 1998; Florindo et al., 2007; Marra et al., 2008, 2013, 2016a, 2016b; Marra and Florindo, 2014; Luberti et al., 2017). An aggradational succession includes different facies, each diagnostic of specific sea-level conditions, tied to a specific stage of a “sawtooth” glacial-interglacial cycle (drawn on the left of each panel). The succession begins with the development of a deltaic plain (a) during an interglacial period, which features sea level standing at or up to a few meters above the present level for several millennia (highstand). Sea (base) level gradually lowers across the ensuing glacial period down to a lowstand at the glacial maximum (b), causing coastline regression, development of a basal erosional surface, valleys to be progressively incised, and sediments to be “bypassed” to the sea. During this phase, coarse gravel is transported along the river channel, but it is continuously removed and deposited offshore, in consequence of the progressive sea-level fall and deepening of the valley incision. The rapid sea-level rise (meltwater pulse) at the glacial termination (c) promotes rapid (abrupt) filling of the Tiber River valleys with a fining-upward sequence of clastic sediments that is characterised by a basal interval of distinct gravel deposition that abruptly switches to clay deposits. Gravel deposition marks the rapid to abrupt sea-level rise during the meltwater pulses, while the fine-grained sediments testify to the sea-level rise that leads to the (interglacial) highstand. Upon return to interglacial climate conditions (d), the sea-level highstand leads to another deltaic plain prior to another cycle. These sedimentary facies become exposed by continuous uplift affecting the Tiber River area that stem from eruptive phases of the regional volcanic districts (e.g., Karner et al., 2001a; Ferranti et al. 2006; Marra et al., 2016b). Blue arrows indicate whether sea level is lowering (downward arrow), rising (upward arrow), and standing (up-down arrow).

1 The intense explosive activity of the regional volcanic districts fed by potassium-rich magma  
2 (Conticelli and Peccerillo, 1992) ensures robust chronological constraints through high-  
3 precision  $^{40}\text{Ar}/^{39}\text{Ar}$  dating of the numerous tephra layers that occur within the sedimentary  
4 successions of the Paleo Tiber River (Alvarez et al., 1995; Karner and Renne, 1998).  
5 Moreover, geochemical fingerprinting of the various eruptive events allows long-distance  
6 correlation among tephra deposits originated from the same eruption (e.g., Giaccio et al.,  
7 2019; Pereira et al., 2020).  
8 The MIS 11 sections that are described in the present work are part of a complex morpho-  
9 stratigraphic setting, several km wide and up to 40 m in thickness, exposed by quarry  
10 excavations in the Tiber delta area. Such outcrops show that the sedimentary deposits  
11 belonging to the San Paolo Formation (Marra and Rosa, 1995; Karner and Marra, 1998) are  
12 constituted by a fining upward succession with a 4-6 m thick basal layer of coarse gravel  
13 (diameter of the pebbles  $\leq 10$  cm) filling the deepest portion of a set of incised valleys  
14 occurring at 25-30 m a.s.l., abruptly passing to a 20-30 m thick silty-clayey package of  
15 sediments with top at  $\sim 55$  m a.s.l. Biostratigraphic, sedimentologic (Conato et al., 1980) and  
16 sequence stratigraphic (Milli, 1997, 2008) investigations have characterized these sediments  
17 as a vertical succession of fluvial (gravel and sand) to coastal and lagoon (silt and clay)  
18 deposits. Overall, these stratigraphic and sedimentological features occur as a ubiquitous,  
19 distinctive tract of the San Paolo Formation, as well as of other similar aggradational  
20 successions of the Paleo Tiber River delta, systematically observable over a wide area. They,  
21 thus, cannot be related to accidental, local change of the hydrological network, but to a  
22 phenomenon acting on a much wider spatial scale, able to drive large scale and near  
23 synchronous change of the depositional processes, such as the sea level change.

24

25

26 ***2.3. Stratigraphy and chronology of the San Paolo Formation (~450-400 ka)***

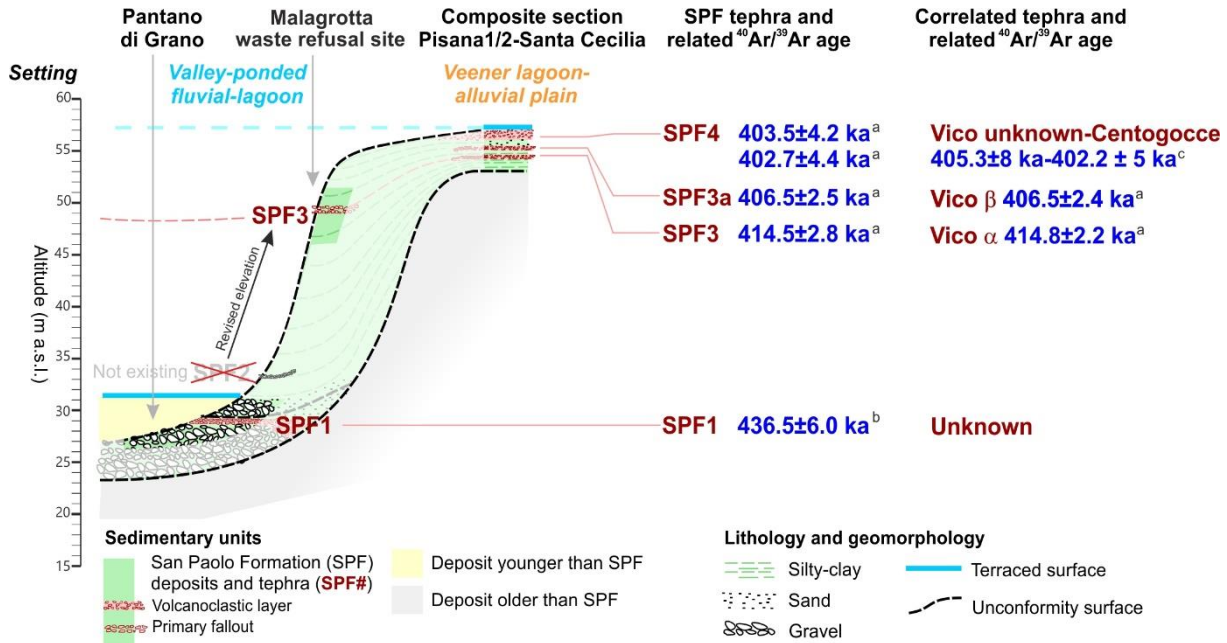


1 The San Paolo Formation (SPF, Karner and Renne, 1998; Karner and Marra, 1998, 2003;  
2 Marra et al., 2016) is a sedimentary succession (Fig. 3) of the Roman coastal area that is  
3 studied here to constrain the timing of the RSL fluctuations during the glacial MIS 12,  
4 termination V (T-V), and the highstand of the interglacial MIS 11. Geochemical and  $^{40}\text{Ar}/^{39}\text{Ar}$   
5 data acquired for the four primary and sub-primary tephra layers (SPF1 through SPF4)  
6 interbedded in the SPF sediments and in the proximal pyroclastic succession of the Vico  
7 Volcano allowed a robust tephrochronological correlation between SPF and Vico Volcano,  
8 resulting in a composite SPF section (Pereira et al. 2020), which reconciled some previous  
9 mis-interpretations (Fig. 3). Specifically, Pereira et al. (2020) revised the altitude, the age, and  
10 the tephrostratigraphic attribution of the tephra layer SPF2 (sample R94-30C) of Malagrotta  
11 waste refusal site, which had previously been dated at  $423.5 \pm 5$  ka, ( $2\sigma$  uncertainties; Karner  
12 and Renne, 1998). Pereira et al. (2020) demonstrated that the layer SPF2 (R94-30C) was  
13 located at higher altitude in the SPF succession and that it correlates with the first Plinian  
14 eruption of Vico Volcano (Vico  $\alpha$ ,  $414.8 \pm 2.2$  ka,  $2\sigma$  uncertainties), and that therefore  
15 matches SPF3 layer (Fig. 3). As consequence, the layer SPF2 was removed from the sketch of  
16 the SPF section that is reported in Figure 3.

17 The other three tephra layers recognized in the SPF sections were labeled SPF1, SPF3a, and  
18 SPF4 and were tephrochronologically constrained as summarized in the following (Fig. 3).

19 The lowermost volcanoclastic layer SPF1 was dated at  $436.5 \pm 6.0$  ka ( $2\sigma$  uncertainties,  
20 Marra et al., 2016), but remained uncorrelated because of the unavailability of samples and  
21 later inaccessibility of the outcrop. The layer SPF3a was instead successfully correlated, by  
22 means of direct  $^{40}\text{Ar}/^{39}\text{Ar}$  dating ( $406.5 \pm 2.5$  ka,  $2\sigma$  uncertainties) and geochemical  
23 fingerprinting, to the second Plinian eruptions of Vico volcano (Vico  $\beta$ ,  $406.5 \pm 2.4$  ka,  $2\sigma$   
24 uncertainties; Pereira et al. 2020). Finally, the complex SPF4 fallout deposit ( $403.5 \pm 4.2$  ka,  
25  $2\sigma$  uncertainties) was interpreted by Pereira et al. (2020) as a result of mixing of two co-

1 eruptive units (Fig. 3) attributable to: (a) an unknown Vico Volcano eruption postdating Vico  
 2  $\beta$ ; and (b) the activity of the Colli Albani Centogocce (following the Pozzolane Nere caldera-  
 3 forming eruption, Marra et al., 2009).



4  
 5 **Figure 3.** Sedimentary, geomorphological, and tephrochronological framework of the  
 6 aggradational succession of San Paolo Formation within the Roman coastal area of Ponte  
 7 Galeria, spanning the MIS 12 through MIS 11 glacial-interglacial transition (modified from  
 8 Pereira et al., 2020). The elevation and the age of what was previously referred as SPF2 layer,  
 9 dated to  $423.5 \pm 5 \text{ ka}$  (Karner and Renne, 1998, sample R94-30C), have been reappraised by  
 10 Pereira et al. (2020), who demonstrated that it actually matches SPF3 layer, correlated to the  
 11 Vico  $\alpha$  eruption dated by these authors to  $414.8 \pm 2.2 \text{ ka}$ . Data source; <sup>a</sup> Pereira et al. (2020); <sup>b</sup>  
 12 Marra et al. (2016); <sup>c</sup> Karner et al., 2001b; Gaeta et al. (2016). All the ages from the literature  
 13 are here recalculated according to the same  $^{40}\text{Ar}/^{39}\text{Ar}$  dating monitor standard for the Alder  
 14 Creek sanidine standard ACs-2 at 1.1891 Ma (Niespolo et al., 2017).  
 15

16

### 17 3. Material and methods

#### 18 3.1. The investigated sections

19 We present new  $^{40}\text{Ar}/^{39}\text{Ar}$  age of a primary volcanic deposit (SAF0, Table 1) intercalated  
 20 within a sedimentary succession cropping out at the Sant'Abbondio section, located  $\sim 35 \text{ km}$   
 21 inland from the present-day coast, within a fluvial tributary valley of the Tiber River (Fig. 1),  
 22 and of the SPF3/R94-30C layer from the coastal SPF sections of Ponte Galeria (Figs. 1 and  
 23 3). Moreover, we present wavelength dispersive spectroscopy (WDS) glass composition of

1 four volcanic units occurring at Sant'Abbondio and at La Rosta sections (Table 1), providing  
 2 two new tephrostratigraphic markers to the SPF aggradational succession. This dataset,  
 3 combined with a review of all existing geochronological and geochemical data, allows a more  
 4 firm constraint on the timing of the aggradational phases and sea-level change during the late  
 5 stage of glacial MIS 12, T-V, and the highstand of interglacial MIS 11. Indeed, in spite of the  
 6 inland location of the Sant'Abbondio section, Marra et al. (2019b) demonstrated how a large  
 7 portion of the catchment basin of the paleo-fluvial system of the Tiber River was sensitive and  
 8 responded synchronously to the sea-level fluctuations, as shown in the case of sections that  
 9 are located even further inland than the Sant'Abbondio section.

10 Stratigraphic logs of the sections investigated in this study are reported in Figure 4, while  
 11 Table 1 summarizes the analysis performed in these sections.

12  
 13 **Table 1.** New and previous  $^{40}\text{Ar}/^{39}\text{Ar}$ , stratigraphic, and wavelength dispersive spectroscopy (WDS) analyses for  
 14 each of the studied sections.

Geological setting	Site/Section	Unit ( $^{40}\text{Ar}/^{39}\text{Ar}$ sample)	Investigations			Latitude and longitude
			Stratigraphy	$^{40}\text{Ar}/^{39}\text{Ar}$ age	WDS glass-composition	
Deltaic succession		SPF3 (R94-30C)	Pereira et al. (2020)	This study	Pereira et al (2020)	41° 51' 00" N 12° 20' 06" E
Fluvial-pyroclastic succession	Sant'Abbondio	SAF1	This study	-	This study	42° 12' 56.67" N 12° 29' 34.61" E
		SAF0	This study	This study	This study	
Monti Sabatini pyroclastic succession	La Rosta	LRF2	This study	Marra et al. (2020)	This study	42° 06' 00.9" N 12° 30' 23.8" E
		LRF1	This study	-	This study	

16  
 17

### 18 **3.2. $^{40}\text{Ar}/^{39}\text{Ar}$ dating**

19 The  $^{40}\text{Ar}/^{39}\text{Ar}$  dating of the Sant'Abbondio Unit Fall 0 (SAF0) and of layer SPF3 (R94-30C)  
 20 were both performed at the Laboratoire des Sciences du Climat et de l'Environnement, Gif-  
 21 sur-Yvette (France). Sample SAF0 was processed using the procedure from Pereira et al.  
 22 (2020) and fully described in Nomade et al. (2010).

1 Sample R94-30C was prepared using the same procedure as in Nomade et al. (2011). Pristine  
2 sanidine crystals ranging in size between 500  $\mu\text{m}$  and 300  $\mu\text{m}$  were handpicked under a  
3 binocular microscope. The sample was irradiated for 120 minutes in the Cd-lined, in core  
4 CLICIT facility of the Oregon State University TRIGA reactor (IRR CO007). Interference  
5 corrections were based on the nucleogenic production ratios given in Balbas et al., (2018).  
6 After irradiation, the individual crystals were transferred into a copper 134 pits sample holder  
7 placed in a differential vacuum Teledyne Cetac window connected to the extraction line.  
8 Minerals were fused one by one using a 100Watts Teledyne Cetac CO<sub>2</sub> laser during 15 s with  
9 a 2.3 W power. Before fusion, each crystal underwent a 10 s sweeping at 0.2 W to remove  
10 unwanted gas trapped superficially. Extracted gases were purified by a SAES GP50 cold  
11 getter for 90s and then for 210 s by two hot SAES GP50 getters. The five Argon isotopes (i.e.,  
12 <sup>40</sup>Ar, <sup>39</sup>Ar, <sup>38</sup>Ar, <sup>37</sup>Ar, and <sup>36</sup>Ar) were simultaneously analyzed using a NGX 600 mass  
13 spectrometer equipped with an array of 9 ATONA Faraday cups and an electron multiplier.  
14 Technical specifications and performances of the NGX 600 ATONA detector array are  
15 presented in Cox et al., (2020). Argon isotopes the following way: in the first run, <sup>40</sup>Ar, <sup>39</sup>Ar,  
16 and <sup>38</sup>Ar were measured simultaneously on 3 ATONA faraday cups, while the <sup>36</sup>Ar was  
17 measured using the electron multiplier. In a second time, after peak switching the <sup>37</sup>Ar was  
18 measured using the electron multiplier. Each isotope measurement corresponds to 15 cycles of  
19 20-seconds integration time. Peak intensity data were reduced using ArArCALC V2.4  
20 (Koppers, 2002). Neutron fluence J for each sample was calculated using co-irradiated Alder  
21 Creek sanidine standard ACs-2 at 1.1891 Ma (Niespolo et al., 2017) according to the K total  
22 decay constant of Renne et al., 2011. To determine the neutron flux of IRR CO007 flux  
23 monitors were placed in small pits framing the sample. Two standards from 3 pits around the  
24 unknown were measured to calculate R94-30C J-value ( $J= 0.0005619 \pm 0.00000045, 1\sigma$ ).  
25 Mass discrimination was monitored by analysis of 30 air pipettes of various beam sizes to  
26 verify the detectors linearity. These measurements are done automatically overnight before

1 and after the unknown measurements (see supplementary material data table). Discrimination  
2 is calculated according to the  $^{40}\text{Ar}/^{36}\text{Ar}$  ratio of 298.56 (Lee et al., 2006). Procedural blank  
3 measurements were achieved after every two or three unknowns depending of the beam sizes  
4 measured previously. For typical 5 min time blank backgrounds are between  $1.7 \cdot 10^{-4}\text{V}$  and  
5  $2.0 \cdot 10^{-4}\text{V}$  for  $^{40}\text{Ar}$  and 65 cps for  $^{36}\text{Ar}$  ( $9.5 \cdot 10^{-7}\text{V}$  equivalent).

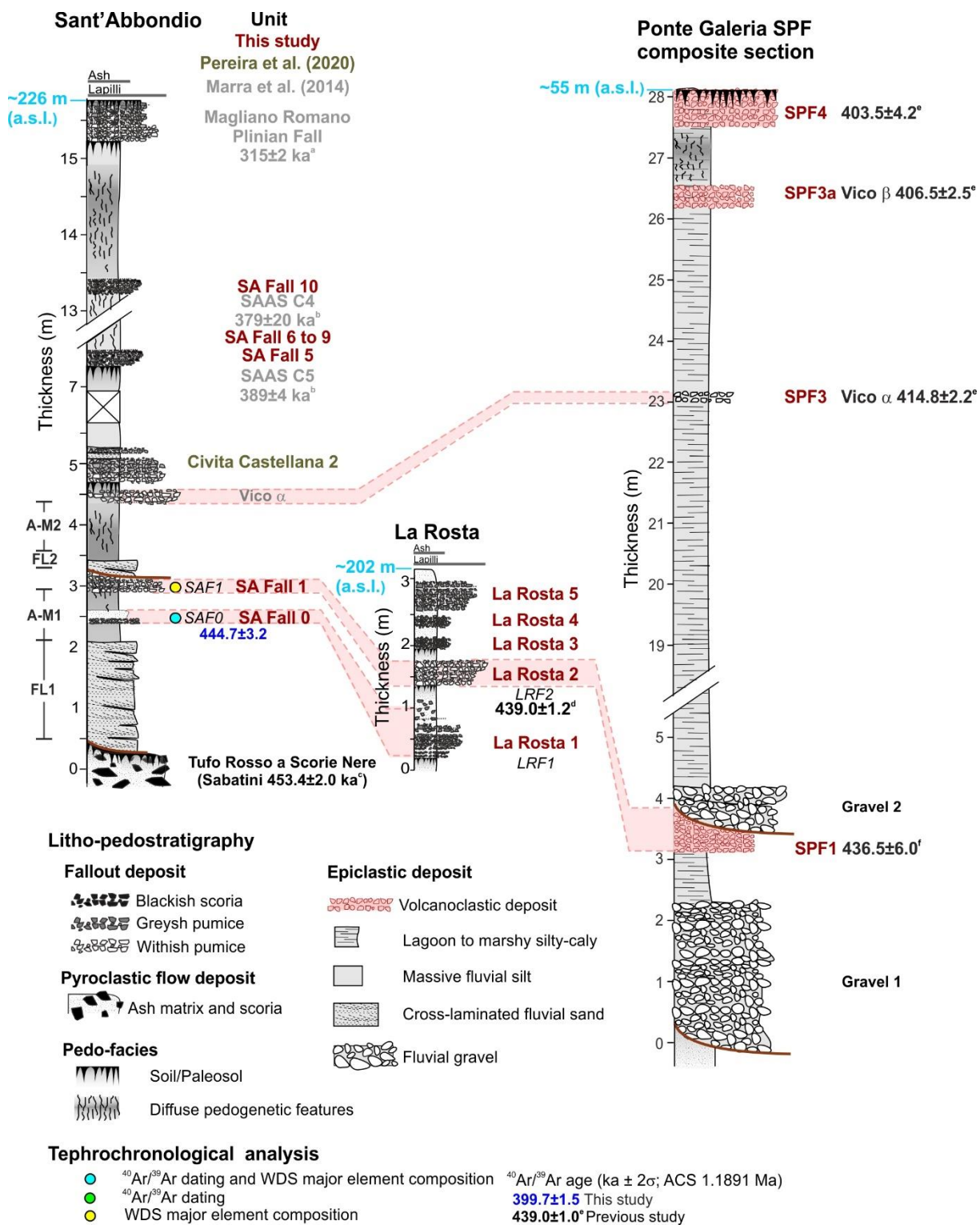
6 New and previously published ages were calibrated against the K total decay constant of  
7 Renne et al. (2011) and the Alder Creek sanidine (ACs-2) optimization calculated standard  
8 age of 1.1891 Ma (Niespolo et al., 2017) was adopted. We retain the optimization calibration  
9 for the age of ACs-2 standard because it presents accurate and quantifiable uncertainties, and  
10 is independent of any astronomical tuning assumptions. Astronomical tuning has inherent  
11 uncertainties that are related, e.g., to the phase relationship between the proxy data and a  
12 specific “tuning target”, such as the insolation curve or a specific orbital parameter (Laskar et  
13 al., 2004). This makes it difficult to quantify the overall chronological uncertainties associated  
14 with the tuned time series, thereby hindering a quantitative comparison with the chronologies  
15 based on  $^{40}\text{Ar}/^{39}\text{Ar}$  dating (Renne et al., 2010). For consistency, all previously published  
16  $^{40}\text{Ar}/^{39}\text{Ar}$  ages are reported with their  $2\sigma$  analytical uncertainties including J and have been  
17 recalculated using the same ACs-2 flux standard age (i.e., 1.1891 Ma).

18

### 19 **3.3. Major element analyses**

20 Major and minor element compositions were determined on interstitial glass of pumices or  
21 scoria of the unit Sant’Abbondio Fall 0 and Fall 1 (SAF0 and SAF1) and La Rosta Fall 1 and  
22 Fall 2 (LRF1 and LRF2) (Table 1). Pumice and/or glass fragments were mounted on slides in  
23 epoxy resin, polished, and carbon coated. Electron microprobe analyser wavelength dispersive  
24 spectroscopy (EMPA-WDS) analyses were performed at the *Istituto di Geologia Ambientale e*  
25 *Geoingegneria* of the Italian National Research Council (IGAG-CNR, Rome). We used a  
26 CAMECA SX-50 EMPA, equipped with a five-wavelength dispersive spectrometer (WDS),

1 and calibrated and set up with the same operating conditions as described in previous studies  
2 (e.g., Giaccio et al., 2017). Analytical precision was evaluated by analyzing in the same run  
3 one external standard (Rhyolite RLS132 glasses from the United States Geological Survey).  
4 Results are shown in supplementary dataset 2 (SD 2). Geochemical analyses yielding  
5 analytical totals <93 wt% were rejected, whereas all analyses with higher totals were  
6 normalized to 100% on a volatile-free basis, that is, excluding Cl, SO<sub>3</sub>, and F volatiles. Glass  
7 shards and micro-pumices were classified according to their geochemical composition using  
8 the Total Alkali vs Silica (TAS) classification diagram (Le Maitre 2002).  
9



1

2 **Figure 4.** Stratigraphic logs of the Sant'Abbondio and La Rosta Sections, investigated in this  
3 study. The sections are correlated with one another and with the San Paolo Formation (SPF),  
4 which is a composite section proposed by Pereira et al. (2020), located in the Roman (Ponte  
5 Galeria) coastal area (sections' locations are shown in Figure 1). The stratigraphic positions of  
6 the samples used either for determining the geochemical composition of volcanic glass or  
7 analyzed for  $^{40}\text{Ar}/^{39}\text{Ar}$  are also shown, while previously published  $^{40}\text{Ar}/^{39}\text{Ar}$  ages are  
8 indicated as follows: (a) Sottili et al. (2010); (b) Marra et al. (2014); (c) Karner et al. (2001b);  
9 (d) Marra et al. (2020); (e) Pereira et al. (2020); (f) Marra et al. (2016).

10

1  
2  
3  
4  
5  
6  
7  
8  
9  
10  
11  
12  
13  
14  
15  
16  
17  
18  
19  
20  
21  
22  
23  
24  
25  
26

## 4. Results

### 4.1 Lithostratigraphy

#### 4.1.2. Sant'Abbondio section - Monti Sabatini Volcanic District

The Sant'Abbondio section consists of a ~15 m thick sedimentary succession of primary pyroclastic fall units ( $n = 10$ ), which are separated by fluvial deposits and/or paleosols that are tephrochronologically constrained between the Monti Sabatini Tufo Rosso a Scorie Nere eruption (TRSN,  $453.4 \pm 2.0$  ka, recalculated in this study from Karner et al., 2001b) and Magliano Romano Plinian Fall ( $313.0 \pm 2.0$  ka; Sottili et al., 2010; Marra et al., 2014) (Figs. 3 and 4). Here we re-examined in detail the basal part of the Sant'Abbondio section that includes the pyroclastic layers SAF0 and SAF1 (Fig. 4).

The basal portion of the Sant'Abbondio section is a fluvial deposit mostly made of volcanoclastic sediments (FL1 in Figs. 4 and 5a), which overlie a deep paleosol that developed on the TRSN pyroclastic-flow (Figs. 4 and 5a). A 5 to 10 cm thick, dark grey, ash and lapilli fallout deposit (SAF0) with a discontinuous ash deposit at the bottom is: (i) intercalated with the fine-grained, upper part of the volcanoclastic deposit (AM-1a); and (ii) overlain by a ~50 cm thick, massive ash-mud deposit (AM-1b). Above the AM-1b sits a 20 to 30 cm thick, white pumice fallout (SAF1), on which deposited another ash-mud layer (AM-1c) that features incipient pedogenesis in the upper portion. Above AM-1c layer, a ~40 cm thick, sand-sized, planar bedded volcanoclastic deposit lays (FL-2), followed by a ~1 m thick, whitish ash-mud deposit (AM-2) capped by a well-developed paleosol (Fig. 5). A discontinuous pumice fallout layer is embedded at the base of this paleosol, which correlates with Vico  $\alpha$  (Marra et al., 2014) that has an age of  $414.8 \pm 2.2$  ka (Pereira et al., 2020). The interval above Vico  $\alpha$  contains a pumice fall deposit, attributed to an unknown eruption of Sabatini (Civita Castellana 2; Pereira et al., 2020), and the so-called Sant'Abbondio Ash fall Succession (SAAS,  $390 \pm 4$  ka, Marra et al., 2014) that is capped by the Magliano Plinian



1 Plinian Fall (Fig. 4). The sedimentary interval comprised between the TRSN and Vico  $\alpha$  at  
2 Sant'Abbondio deposited between  $\sim 453$  ka and  $\sim 415$  ka and is therefore coeval with the basal  
3 portion of the San Paolo Formation exposed in the Roman coastal area, i.e., the Pantano di  
4 Grano and Malagrotta Sections (Fig. 3).

5

#### 6 *4.1.3. La Rosta section - Monti Sabatini Volcanic District*

7 The fallout succession exposed in La Rosta has been recently investigated by Marra et al.  
8 (2020). It consists of five pyroclastic units separated by incipient paleosols, overlain by the  
9 Magliano Romano Plinian fall ( $313.0 \pm 2.0$  ka, Sottili et al., 2010). The pumice fall La Rosta  
10 2 (LRF2 in Fig. 4) was recently  $^{40}\text{Ar}/^{39}\text{Ar}$  dated ( $439.0 \pm 1.2$  ka, recalculated in this study  
11 from Marra et al., 2020) and was potentially sourced in the central Sabatini Volcanic District  
12 (Marra et al., 2020).

13 The lowest unit (LR-1) of the La Rosta fall succession comprises a basal, 3 cm thick, dark  
14 grey ash-surge layer (LRS1), which is followed by a 12 cm thick lapilli fallout (LRF1) and by  
15 a 10 cm thick, ash-lapilli pyroclastic-flow deposit (LRP1) (Figs. 4 and 5b). A 30 cm thick,  
16 inversely graded, up to 3 cm in diameter holocrystalline lithic fallout layer (LRH1) closes the  
17 lower eruptive sequence at the top (Figs. 4 and 5b). Above a 40 cm-depth pedogenized ash  
18 layer, the eruptive unit (LRF2) consists of a  $\sim 35$  cm-thick Plinian fallout made up of whitish,  
19 well vesicular, subaphyric pumice lapilli and includes a basal  $\sim 5$  cm thick bed with abundant  
20 lava lithics. The Plinian unit LRF2 is overlain by three minor units composed by decimeter-  
21 thick ash layers and black, leucite-bearing (often analcimized) scoria lapilli fall deposits, rich  
22 in lava lithic inclusions and holocrystalline lithic clasts, the uppermost of which is  $\sim 60$  cm  
23 thick (LRF3 to LRF5; Figs. 4 and 5b).

24

25

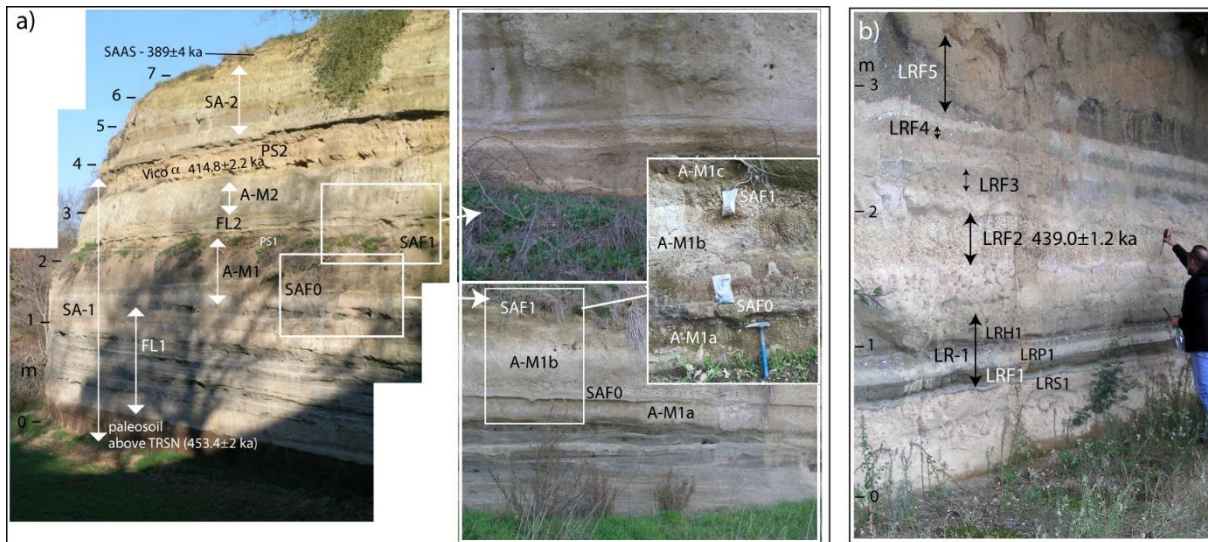


**Figure 5.** Pictures of the investigated Sant' Abbondio and La Rosta sections. **a)** General view (left picture) and details (right pictures) of the basal interval of the MIS 11 Sant' Abbondio section ( $42^{\circ} 12' 56.67''$  N,  $12^{\circ} 29' 34.61''$  E; elevation: 226 m a.s.l.), including the SAF0 and SAF1, lying on the paleosol developed on the Tufo Rosso a Scorie Nere (TRSN). **b)** General view of the La Rosta section including the investigated LRF1 and LRF2 units ( $42^{\circ}06'00.9''$ N,  $12^{\circ}30'23.8''$ E; elevation: 202 m a.s.l.).

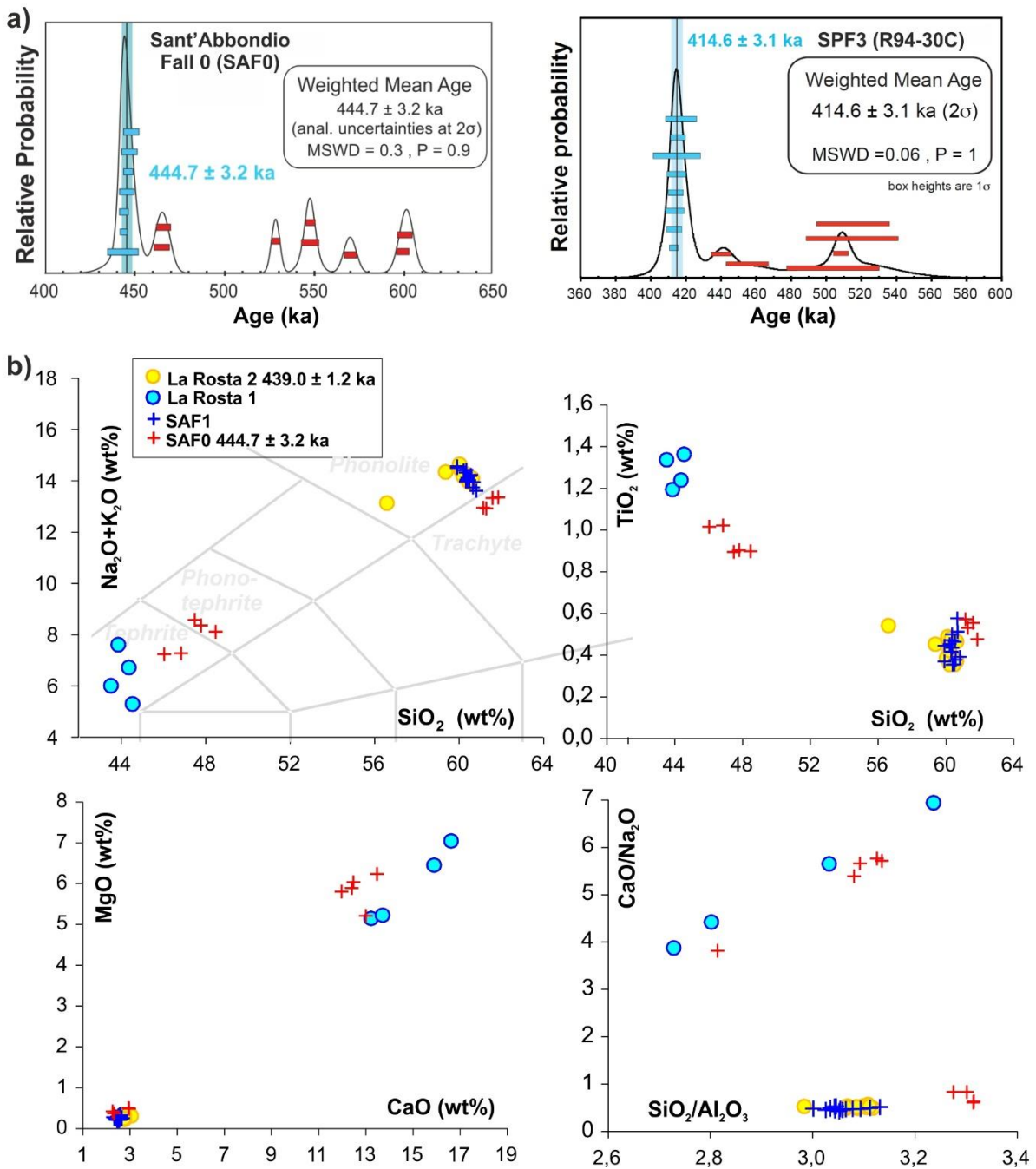
#### 4.2. $^{40}\text{Ar}/^{39}\text{Ar}$ dating

Fifteen crystals of both sanidine and leucite from Sant' Abbondio Fall 0 (sample SAF0, Fig. 4, Table 1) were  $^{40}\text{Ar}/^{39}\text{Ar}$  dated (supplementary dataset 1, SD 1). The relative probability diagram of this sample is multimodal (Fig. 6a) and reflects multiple crystal age populations. The youngest population contains seven crystals, allowing to calculate a weighted mean age of  $444.7 \pm 3.2$  ka, MSWD = 0.3 and P= 0.9. The  $^{40}\text{Ar}/^{36}\text{Ar}$  initial ratio given by the inverse isochron is of  $299.6 \pm 3.4$  ka, equivalent to the atmospheric one of 298.56 ka (Lee et al., 2006), confirms the absence of argon excess or of argon fractioning in the sample.

The relative probability diagram of sample R94-30C is multimodal like SAF0, indicating clearly several populations of contaminating xenocrysts, ranging between  $440.7 \pm 11.4$  ka up to  $521.8 \pm 37.6$  ka (Fig. 6a). The youngest population contains eight crystals, allowing to calculate a valid weighted mean age of  $414.6 \pm 3.1$  ka ( $2\sigma$ , MSWD = 0.06 and P = 1.0; Fig.

1 6a). The  $^{40}\text{Ar}/^{36}\text{Ar}$  initial ratio given by the inverse isochron is  $298.7 \pm 3.0$  ka, identical within  
 2 uncertainties with the atmospheric reference of 298.56 (Lee et al., 2006), showing no excess  
 3 argon in this population. The new age we present here for the layer SPF3 (R94-30C) at  $414.6$   
 4  $\pm 3.1$  ka is consistent with that of Vico  $\alpha$  ( $414.8 \pm 2.2$  ka; Pereira et al., 2020) and confirms  
 5 the previous correlation based on geochemical composition (Pereira et al., 2020).

6



7

1 **Figure 6.** Age and geochemistry of the investigated tephra layers. **a)** Single grain  $^{40}\text{Ar}/^{39}\text{Ar}$   
2 age of SAF0 and SPF3 (R94-30C) on single grain presented as probability diagram; **b)** total  
3 alkali *versus* silica diagram (Le Maitre, 2002) and representative bivariate diagrams for the  
4 tephra from the La Rosta (LRF1 and LRF2) and Sant'Abbondio (SAF0 and SAF1) sections.  
5

### 6 **4.3. Geochemical composition of the tephra from Sant'Abbondio and La Rosta sections**

7 Full glass compositions are provided in supplementary dataset 2 (SD 2), while their  
8 classification according to the Total Alkali *versus* Silica (TAS) is shown in Figure 6b.

9 *Sant'Abbondio Fall 1 and Fall 2* – The composition of the glass from SAF0 is highly  
10 scattered, ranging from poorly differentiated tephritic and phono-tephrite terms, with MgO  
11 contents of up to 6 wt% (Fig. 6b) to an evolved trachyte composition with a silica content of  
12 ~61–62 wt% and ~13 wt% of alkali sum (Fig. 6b). The glass in SAF1 has instead an almost  
13 homogeneous phonolitic composition with SiO<sub>2</sub> contents of ~60–61 wt% and alkali sum of  
14 ~13.5–14.5 wt% (Fig. 6b).

15 *La Rosta Fall 1 and 2* – The few analyzable glass shards found in the microlithic-rich juvenile  
16 clasts of LRF1 have a primitive tephrite composition, with a SiO<sub>2</sub> content of ~44 wt% (Fig.  
17 6b) and a MgO contents as high as 7 wt% (Fig. 6b), similar to the primitive component of  
18 SAF1. The LRF2 pumice fall is instead characterized by a homogeneous phonolitic  
19 composition with SiO<sub>2</sub> content of ~60–61 wt% and alkali sum of ~13.5–14.5 wt%, similar to  
20 SAF1 (Fig. 6b).

21

## 22 **5. Discussion**

### 23 **5.1. Correlation of inland and costal sections of the San Paolo Formation**

24 The two pairs of pyroclastic units of the Sant'Abbondio and La Rosta sections investigated  
25 here (i.e., SAF0-SAF1 and LRF1-LRF2, Figs. 3 and 4) share similar stratigraphic and  
26 textural-lithological features, and geochemical composition. New and/or revised  $^{40}\text{Ar}/^{39}\text{Ar}$   
27 dating of these units brackets the interval between  $444.7 \pm 3.2$  ka and  $439 \pm 1.2$  ka.

1 Specifically, the tephritic and phono-tephritic components of the heterogeneous SAF0 share a  
2 high degree of similarity with the La Rosta Fall 1 (i.e., LRF1), while the homogenous  
3 phonolitic glass composition of the white pumices from SAF1 precisely matches that of the  
4 La Rosta Fall 2 (i.e., LRF2, Fig. 6b-c). Therefore, stratigraphic order, lithology, and  
5 geochemical composition collectively suggest that the units from Sant'Abbondio and La  
6 Rosta sections can be confidently correlated with one another. This correlation also provides a  
7 refined and more precise geochronological constraint for the deposition of the SPF1 pumice  
8 layer of the basal part of Pantano di Grano section in Ponte Galeria for which the outcrop is  
9 no longer accessible but was previously dated at  $436.5 \pm 6.0$  ka (Marra et al., 2016a). The age  
10 of the SPF1 collected at Pantano di Grano is statistically indistinguishable from that of LRF2  
11  $439.0 \pm 1.2$  ka. Also in terms of textural and lithological features, SPF1 is consistent with  
12 LRF2, as in the original field notes collected by one of us (F.M.) it is described as “a cross-  
13 bedded volcanic sand, prevalently made of mm-sized white pumice and loose pyroxene  
14 crystals”, similar to LRF2. Therefore, by transferring the age of  $439.0 \pm 1.2$  ka from La Rosta  
15 Fall 2 to SPF1 (Figs. 4 and 7) we (i) overcome the problems associated with inaccessibility of  
16 the outcrop and the associated lack of samples for  $^{40}\text{Ar}/^{39}\text{Ar}$  dating and geochemical  
17 fingerprinting and (ii) substantially improve the precision of the dating of this SPF tephra.

## 19 ***5.2. Paleo Tiber River aggradational successions as a proxy for sea-level rise and*** 20 ***significance of the basal coarse-grained sediments***

21 The aggradational successions of the Paleo Tiber River consist each of a fining upward  
22 sequence (gravel, sand, silt, and clay) that deposit upon an unconformity surface (Karner and  
23 Marra, 1998). Following the conceptual model developed by Marra et al. (2008, 2016a), these  
24 successions provide a stratigraphic record (i.e., a full transgression cycle) of past glacial-  
25 interglacial sea-level cycles, while the “switch” from the coarse-grained (gravel) intervals at

1 the base of these successions to the fine-grained (silt and clay) intervals at the top are  
2 diagnostic of rapid (abrupt) sea-level rise (meltwater pulses) at glacial terminations (Fig. 2).  
3 In all the analyzed cases we deal with a chrono-morpho-stratigraphic context including:  
4 i- an unconformable boundary between a pre-aggradational geologic substrate and an  
5 overlying fining-upwards (aggradational) fluvial succession;  
6 ii- tight geochronologic constraints evidencing that the unconformable boundary corresponds  
7 to an erosional phase coeval with a sea-level lowstand;  
8 iii- a dm- to m-thick coarse sedimentary deposit (generally ascribable to well graded clean  
9 gravel and sand: GWSW, according to the Unified Soil Classification System) directly above  
10 the erosional surface, abruptly transitioning vertically over a few centimeters (jumping several  
11 divisions of sediment classified in the Unified Soil Classification System) to a several m-  
12 thick, fine-grained sedimentary package (i.e., high plasticity silt and clay with organic clay:  
13 CHOMH) (Marra et al., 2013).

14 Several lines of evidence support this interpretative model and, in turn, the reconstructions of  
15 the timing of ice-sheet melting during the late stages of glacial MIS 12 and at T-V based on  
16 the analysis of SPF aggradational successions presented in this study. First, conditions for the  
17 accumulation of the coarse gravel deposit only (co)existed at the onset of glacial terminations  
18 due to the: (i) low sea level at glacial maxima (e.g., Lambeck et al., 2014; Rohling et al.,  
19 2017; Yokoyama et al., 2018), which steepens the gradients and, in turn, enhances the river  
20 competence (Fig. 2b-c); (ii) rapid melting of Apennine glaciers (Giraudi and Frezzotti, 1997)  
21 that releases large amount of clastic material, thereby increasing the sediment supply to the  
22 Tiber drainage basin; and (iii) overall increase in regional precipitation (Wagner et al., 2019).  
23 Second, the abruptness of the “sedimentary switch” that marks the transition from the gravel  
24 bed (up to ~10 m in thickness), through a thin (1–2 m in thickness) sand bed, into the thick  
25 (>30 m in thickness) silt and clay section claims for the sudden establishment of a low  
26 gradient, consistent with fast sea-level rise (meltwater pulse) and subsequent development of

1 a sea-level highstand (Fig. 2d), in line with the observations across glacial termination I  
2 (Marra et al., 2008, 2013, 2016). Third, there is an excellent agreement between the timing of  
3 meltwater pulses inferred from the Paleo Tiber River aggradational successions (Marra et al.,  
4 2008, 2016), the rates of sea-level rise obtained from continuous, radiometrically constrained  
5 sea-level records (Grant et al., 2014), and the glacial termination ages in deep-ocean benthic  
6 foraminiferal  $\delta^{18}\text{O}$  (Lisiecki and Raymo, 2005). This temporal consistency is particularly  
7 strong and convincing for the most recent Late Glacial-Holocene transition, which is  
8 constrained by  $^{14}\text{C}$  dating and provides a proof of concept for the sedimentary model of Marra  
9 et al. (2008, 2016a). These studies highlight the agreement within uncertainties of the timing  
10 of deposition for the basal gravel of the most recent Tiber delta aggradational succession  
11 (between  $15.0 \pm 0.1$  ka and  $12.8 \pm 0.1$  ka) with the Bølling warming and MWP 1a  
12 (Deschamps et al., 2012; Brendryen et al., 2020). [While abrupt stratigraphic changes may](#)  
13 [have purely climatic forcing \(e.g., Blum et al., 1994\), the coupled effect of climate and sea-](#)  
14 [level change in this case is straightforward as evidenced by coincidence with the meltwater](#)  
15 [pulse \(see Figure 1c in Marra et al., 2016\).](#)

16 Fourth, Early *versus* Middle to Late Pleistocene successions exhibit markedly differently  
17 thicknesses of the respective clay sections (Karner et al., 2001a; Marra et al., 2008, 2013,  
18 2016a). The increasing thickness of the clay sections through Early-Middle Pleistocene  
19 represents the plausible sedimentary response of the Paleo Tiber River to the higher  
20 amplitude, rapid terminations of the “sawtooth cycles” occurring after the Middle Pleistocene  
21 Transition and the Mid-Brunhes event (Jansen et al., 1986; Clark et al., 2006; Elderfield et al.,  
22 2012; Barth et al., 2018; Ao et al., 2020).

23 Finally, a tectonic origin (i.e., fault displacement) of these successions could be excluded,  
24 given that the gravel horizons systematically occur at the base of the aggradational sections  
25 and rest above an unconformable surface, which marks the intervening erosional phase during  
26 the sea-level lowstand at glacial maxima. Moreover, in a region as far as 100 km from the

1 Apennines carbonate mountains, representing the source area for the coarse gravel sediment,  
2 fault displacement would cause an abrupt increase of accommodation space, along with a  
3 sudden drop in river transport capacity. Such elements rather cause the deposition of fine-  
4 grained, clayey deposits, as shown for the case of the Paleo-Tiber graben (Marra and  
5 Florindo, 2014).

6

### 7 ***5.3. Chronology of rapid ice-sheet melting prior to and during T-V, and relationship with*** 8 ***insolation***

9 In the coastal setting of the Ponte Galeria area, the volcanoclastic SPF1 deposit (equivalent to  
10 LRF2 in La Rosta section, see above) is found in between a fine-grained horizon and an  
11 erosion surface (unconformity) that separates two distinct gravel layers (Gravel 1 [G1] and 2  
12 [G2], Fig. 4), thereby indicating a maximum age of  $439.0 \pm 1.2$  ka for the unconformity that  
13 underlies G2 (Fig. 7). Similarly, in the Sant'Abbondio section the pyroclastic level SAF1,  
14 equivalent to the SPF1, is sandwiched in between two cross-laminated coarse sand beds (FL-1  
15 and FL-2, Figs. 3, 5a and 7) that are separated by a fine-grained level (A-M1 in Figs. 3, 5a  
16 and 7) and an unconformity (Fig. 7). A low-energy sedimentary environment is then re-  
17 established above FL-2 and capped with the Vico  $\alpha$  pumice fall, indicating that deposition of  
18 the upper aggradational succession of SPF ended at  $414 \pm 8$  ka.

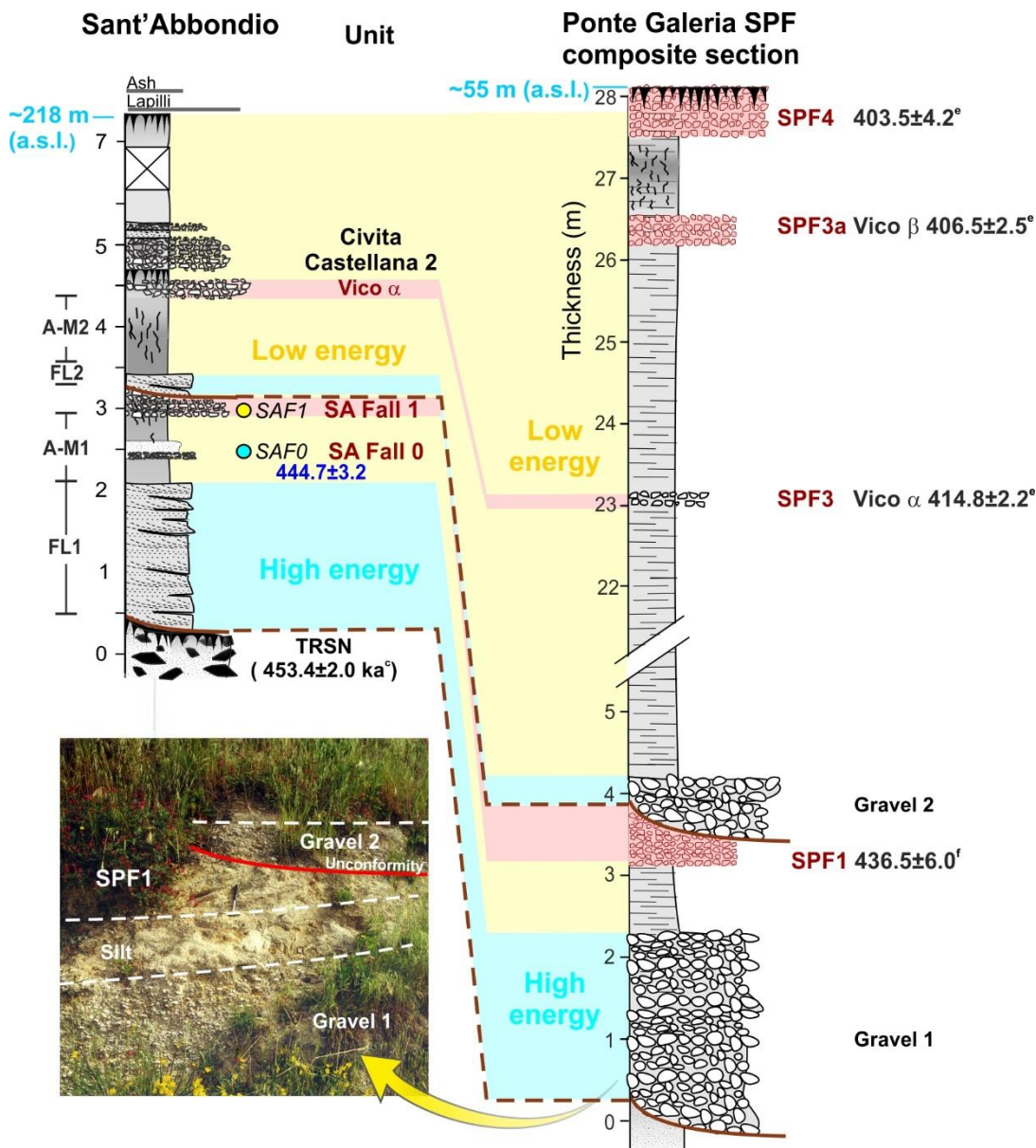
19 In summary, based on the similarity between the sequence of depositional and pedogenic-  
20 erosional events, constrained by the La Rosta 2 Fall and Vico  $\alpha$  tephra layers, we can  
21 reasonably assume that the alternation of coarse- and fine-grained sediments observed at the  
22 Sant'Abbondio sections are the inland, fluvial counterpart of the high- and low-energy  
23 lithofacies of the SPF deposits found in the coastal setting of the Ponte Galeria area (Fig. 7).  
24 Specifically, the sand layers FL1 and FL2 at Sant'Abbondio section testify to sediment  
25 deposition in a high-energy setting and are interpreted here as the inland counterpart of (hence  
26 contemporaneous to) the coastal gravel levels G1 and G2 found in the coastal setting of Ponte



1 Galeria (Fig. 7). In the following, we build on these findings to refine the chronology of the  
2 sea-level change during the last stages of MIS12 and MIS11, using the aggradational  
3 successions of Sant'Abbondio section.

4 The occurrence of the Sabatini TRSN eruption products dated at  $453.4 \pm 2.0$  ka (recalculated  
5 in this study from Karner and Renne, 1998) at the very bottom of the Sant'Abbondio section  
6 adds an additional chronological constraint (i.e., a maximum age) to the onset of deposition of  
7 the basal gravel level G1 and its equivalent coarse sand layer FL1 at Sant'Abbondio that is  
8 capped by SAF0 ( $444.7 \pm 3.2$  ka). Considering the partial erosion and pedogenesis of the  
9 TRSN, we argue that G1 deposition plausibly occurred between  $\sim 450$  ka and  $\sim 445$  ka, which  
10 we take as the timing of a meltwater pulse event (i.e., MWP1, Fig. 8a). MWP1 coincides with  
11 the positive rates of sea-level change in the continuous, radiometrically constrained sea-level  
12 record of Grant et al. (2014, Fig. 8b,c)) that is based on the "Red Sea method" (Siddall et al.,  
13 2003). This corroborates our finding and further highlights the sensitivity of the Paleo Tiber  
14 River aggradational successions to sea-level rise (Marra et al., 2008, 2016a). In addition,  
15 MWP1 occurred under the deep glacial boundary conditions of MIS 12 and preceded by up to  
16  $\sim 23$  kyr the onset of T-V, for which the timing has also been radiometrically constrained  
17 using speleothem time series (Cheng et al., 2016).

18



1

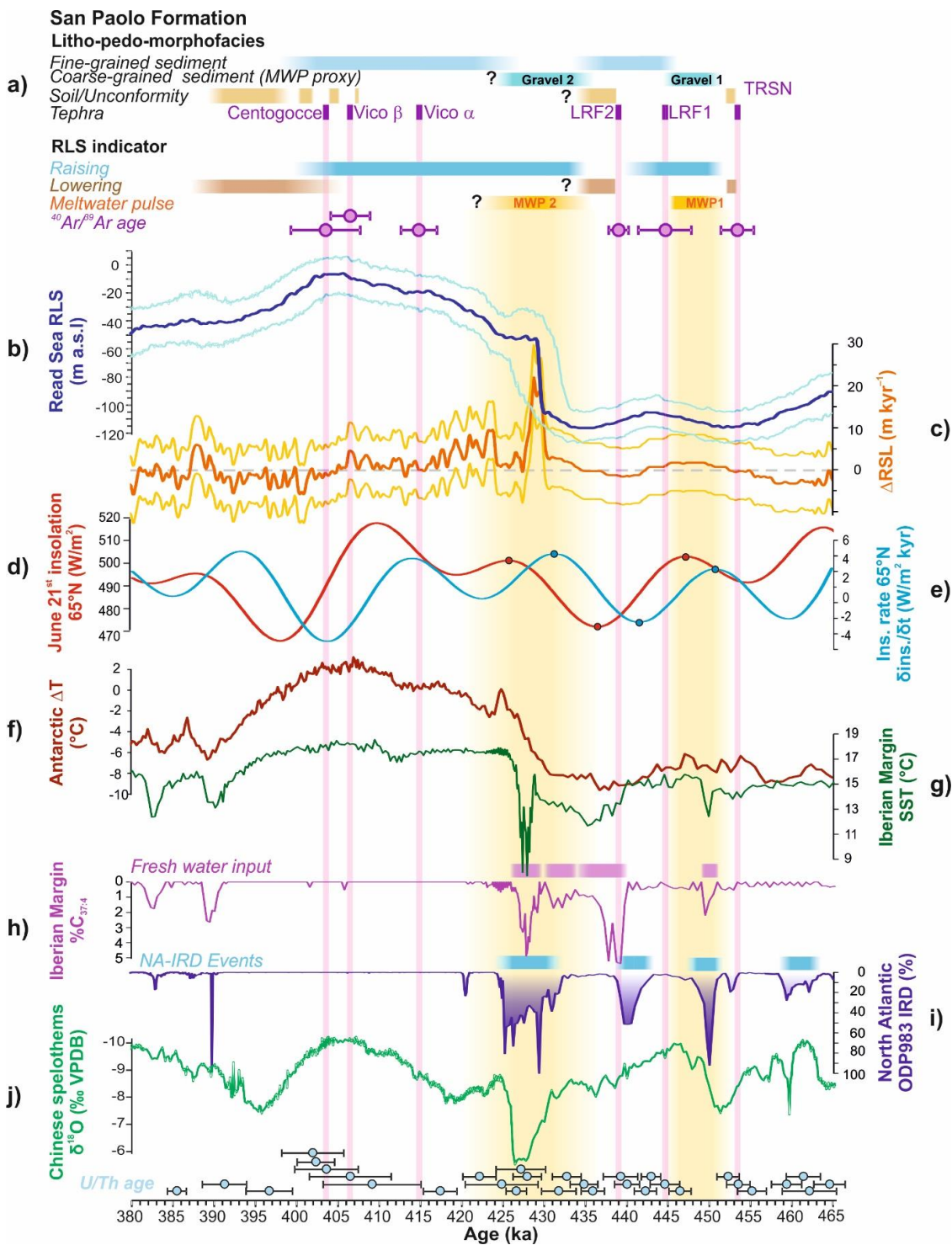
2 **Figure 7.** Stratigraphic and tephrochronological correlations between the Sant'Abbondio  
 3 section and San Paolo Formation (SPF) composite section in the Roman, Ponte Galeria,  
 4 coastal areas. The blue and yellow bands indicated the high-energy and low-energy  
 5 lithofacies, respectively. A picture of the basal portion of the SPF, outcropping at Pantano di  
 6 Grano, is also shown. Litho-pedo-morphostratigraphic symbols as in Figure 4.  
 7

8 The lower chronological limit of  $439.0 \pm 1.2$  ka for the unconformity at the base of the upper  
 9 gravel layer (G2) in the Ponte Galeria coastal area (see above) points to a multi-millennial  
 10 scale return to more glaciated conditions (lowering sea level) that postponed deposition of  
 11 SAF1 (equivalent to LRF2 and SPF1, Figs. 4 and 7) and promoted a drop in base level and  
 12 attendant incision of the Paleo Tiber River valleys (Marra et al., 2008, 2016a). This sea-level

1 drop marked the descent into the “glacial maximum” of MIS 12 that preceded a second  
2 meltwater pulse event (MWP2) that can be ascribed to T-V (Fig. 8). The La Rosta 2 ( $439.0 \pm$   
3  $1.2$  ka) and Vico  $\alpha$  ( $414.5 \pm 2.8$  ka) pumice fall horizons bracket the timing of MWP2 in our  
4 sections (Figs. 7 and 8). The upper and lower chronological limits of MWP2 cannot be further  
5 narrowed in the Paleo Tiber River aggradational successions, because: (a) a previously  
6 reported age constraint for the intermediate SPF2 layer ( $423.5 \pm 5.1$  ka, Marra et al., 2016a;  
7 Fig. 3) has been dismissed; and (b) the occurrence of LRF2 below the basal unconformity of  
8 G2 marks the timing of sea-level drop and provides no direct constraint to the timing of the  
9 meltwater pulse. However, we note that this age window ( $\sim 439$ - $415$  ka) encompasses the T-  
10 V, marked by the maximum rate of sea-level rise reported by Grant et al. (2014) and centered  
11 at  $\sim 430$  ka (Fig. 8). Therefore, in light of this broad chronological agreement and by analogy  
12 with other well constrained events of gravel deposition (e.g., Marra et al., 2016), it is  
13 reasonable to assume that gravel level G2 deposited during the rapid (or even abrupt) sea-  
14 level rise (meltwater pulse) of T-V. Following T-V, continuous sedimentation in the SPF  
15 coastal plain sections at Ponte Galeria alludes to moderate sea-level rise until  $\sim 403$  ka, when  
16 erosion or pedogenesis mark the onset of the sea level lowering and the beginning of the MIS  
17 11b substage, consistent with the Red Sea record (Grant et al., 2014, Fig. 8b).

18 The sequence of events at the MIS 12 to MIS 11 transition, characterized by two episodes of  
19 rapid ice-sheet melting during late MIS 12 and at T-V, separated by a brief interval of ice-  
20 volume growth, parallels relatively subtle changes ( $10 \text{ W m}^{-2}$  to  $\sim 30 \text{ W m}^{-2}$ ) in summer  
21 insolation at the critical latitude of  $65^\circ\text{N}$  (Laskar et al., 2004; Fig. 8d). Specifically, ice-sheet  
22 melting and growth appear to coincide with positive and negative peaks, respectively, in the  
23 (rates of) insolation (change), with higher rates at MWP2 (i.e., T-V) than at MWP1 (Fig. 8d-  
24 e). This observation agrees with the notion that higher rates of insolation change may  
25 contribute to force a complete transition from glacial to interglacial climate states (Cheng et  
26 al., 2009), while it also suggests a potential role of negative insolation rates on ice-sheet

1 growth.



2

3 **Figure 8.** Evidence of insolation, sea-level, and climate changes during the MIS 12 to MIS 11  
 4 transition. **a)** Main litho-pedo-stratigraphic and morphological features with related Relative  
 5 Sea Level (RSL) indicators and <sup>40</sup>Ar/<sup>39</sup>Ar geochronology of the San Paolo Formation  
 6 aggradational succession. Note that tephra units are reported with their formal eruption  
 7 names, regardless the dated sample labels. **b)** and **c)** relative seal level (RSL) change and rates  
 8 of RSL change based on the “Red Sea method” (Grant et al., 2014). **d)** and **e)** June 21<sup>st</sup>  
 9 insolation and insolation rates at 65°N (Laskar et al., 2004). **f)** Antarctic atmospheric  
 10 temperature EPICA Dome C ice core (Jouzel et al., 2007). **g)** Iberian Margin Sea surface

1 temperature (SST) variability at the Iberian Margin core MD03-2699 (Rodrigues et al., 2011).  
2 **h)** Percentage of tetraunsaturated ( $C_{37:4}$ ) alkenones indicative of cold and potentially fresh  
3 surface waters at the Iberian Margin core MD03-2699 (Rodrigues et al., 2011). **i)** Ice-rafted  
4 debris (IRD) record from the North Atlantic Ocean Drilling Program (ODP) Site 983 (Barker  
5 et al., 2019). **j)** Chinese speleothem composite stable oxygen isotope ( $\delta^{18}O$ ) time series. U/Th  
6 dating and associated  $2\sigma$  uncertainties are also shown (Cheng et al., 2016).  
7

#### 8 **5.4. Paleoclimate implications**

9 The coupling of (rates of) insolation changes and ice-volume variations that we report for the  
10 MIS 12 to MIS 11 transition lends supports to the astronomical theory that ascribes the  
11 Northern Hemisphere ice-sheet melting to variations in the orbital parameters that control the  
12 insolation at the top of the atmosphere (Milanković, 1941; Imbrie and Imbrie, 1980; Paillard,  
13 2001). Other studies have related the glacial-interglacial ice-volume (sea-level) changes to  
14 polar climate, and more specifically to changes in Antarctic air temperatures on both glacial-  
15 interglacial and millennial timescales (e.g., Shackleton et al., 2000; Siddall et al., 2003). This  
16 notion has provided the basis to “tune” the continuous sea-level reconstructions obtained from  
17 Red Sea sediment cores to Antarctic temperature records (Rohling et al., 2009). Subsequent  
18 construction of a radioisotopically constrained chronology for the same sea-level record has  
19 provided independent evidence for the close coupling of Antarctic temperatures and sea-level  
20 changes over the last ~500 kyr (Grant et al., 2014). An intermediate complexity model  
21 supported by paleoceanographic data through the last glacial cycle indicates that sea-level rise  
22 may arise from bipolar meltwater releases (Rohling et al., 2004). However, later studies  
23 concluded that insolation-forced Northern Hemisphere ice-sheet melting and Antarctic  
24 temperature rise may be explained by the so-called “bipolar seesaw” (Stocker and Johnsen,  
25 2003), which, in turn, arises from the perturbation of the Atlantic Meridional Overturning  
26 Circulation linked meltwater release into the North Atlantic (Cheng et al., 2009; Barker et al.,  
27 2011). This causes asynchronous temperature and ice-sheet melting across the hemispheres  
28 (Marino et al., 2015; Rohling et al., 2019). The sequence of ice-volume (sea-level) changes  
29 documented here for the MIS 12 to MIS 11 transition fits this picture.

1 Meltwater pulses MWP1 (~450-445 ka) and MWP2 (~430 ka) occurred during periods of  
2 North Atlantic cooling and freshening (Fig. 8g, h) associated with the deposition of ice-rafted  
3 debris (IRD, Fig. 8i), equivalent to the so-called Heinrich events (Hemming, 2004), the  
4 weakening of the Asian Monsoon exemplified by positive shifts in the radioisotopically dated  
5 isotopic record of the Chinese speleothems (Fig. 8j), and the Antarctic warming (Fig. 8f). The  
6 occurrence of prominent IRD peaks associated with these meltwater pulses alludes to  
7 episodes of extensive iceberg calving in the North Atlantic, consistent with sustained melting  
8 of the circum-North Atlantic ice sheets (McManus et al., 1999) during both events. The  
9 occurrence of two, precisely dated tephra units bracketing the deposition of gravel level G1 in  
10 SPF allow a precise timing of the MWP1 (450-445 ka) reported here. However, we note that  
11 the rates of sea-level rise during MWP1 are quite modest (~1.6 m/kyr), compared with the  
12 maximum value of ~20 m/kyr observed at ~430 ka during MWP2 (Fig. 8c). The subdued rates  
13 of sea-level change in the record of Grant et al. (2014) during MWP1 may therefore be  
14 attributed to the lack of firm age constraints in this record that cause an apparent “relaxation”  
15 of the reconstructed rates of sea-level change. Note that this is plausible given that the  
16 chronology of the sea-level record of Grant et al. (2014) is better constrained at glacial  
17 terminations, where their approach (i.e., the synchronization of dust peaks in their sediment  
18 cores to the weak monsoon events of Cheng et al., 2009) exploits the large amplitude of the  
19 signals (higher signal to noise ratios). As for the deposition of the gravel level G2, although  
20 less precisely constrained by the available  $^{40}\text{Ar}/^{39}\text{Ar}$  dating of the SPF succession, the  
21 coincidence with the high rates of sea-level change in the record of Grant et al. (2014) and  
22 with a distinct bipolar seesaw signature of the various paleoclimate records (Fig. 8) lends  
23 confidence to our interpretation that it reflects the rapid ice-sheet melting of T-V.

24

## 25 **6. Concluding remarks**

1 We refined the structure timing of the sea-level change at the transition between glacial MIS  
2 12 and interglacial MIS11, by documenting an episode of ice-sheet melting in late MIS12 that  
3 preceded further continental ice growth prior to the extensive ice-volume decrease of T-V.  
4 Our study builds on new stratigraphic, geochemical, and geochronological analysis of two  
5 sections of the inland-coastal composite record of the San Paolo Formation “aggradational  
6 succession” of the Paleo Tiber River. The occurrence of two coarse-grained deposits at the  
7 base of these  $^{40}\text{Ar}/^{39}\text{Ar}$  dated aggradational successions points to two distinct episodes of  
8 rapid sea-level rise – so-called meltwater pulses – that occurred at ~450–445 ka (MWP 1) and  
9 ~439–415 ka (MWP2), respectively. Comparison with radioisotopically constrained,  
10 continuous sea-level time series based on the so-called “Red Sea method” corroborates our  
11 findings and helps to further narrow the timing of MWP2 at ~430 ka. MWP2 coincided with  
12 T-V, the largest amplitude glacial termination of the last millions of years. On sub-orbital  
13 timescales, MWP 1 and MWP2 coincided with two bipolar seesaw events, expressed by  
14 Antarctic warming in response to North Atlantic Ocean freshening (due to meltwater release)  
15 and cooling. The timing of sea-level changes at the MIS 12 to MIS 11 transition appears  
16 closely coupled with that of Northern Hemisphere (rates of) summer insolation change, albeit  
17 the amplitude the insolation changes is relatively small ( $10 \text{ W m}^{-2}$  to  $\sim 30 \text{ W m}^{-2}$ ). Feedback  
18 processes and/or high ice-sheet sensitivity to insolation (rates of) changes must therefore be  
19 considered to explain the ice-volume changes at the MIS 12 to MIS 11 transition.

20

## 21 **Acknowledgments**

22 We thank Cornel Olariu and an anonymous reviewer for providing insightful comments and  
23 suggestions that helped to improve clarity and quality of the paper.

24 G.M. acknowledges support from the University of Vigo’s programme to attract  
25 excellent research talent, a Beatriz Galindo Fellowship (2020), and a generous start-up  
26 package.

1  
2  
3  
4  
5  
6  
7  
8  
9  
10  
11  
12  
13  
14  
15  
16  
17  
18  
19  
20  
21  
22  
23  
24  
25  
26  
27  
28  
29

## References

Alley, R.B., Clark, P.U., Huybrechts, P., Joughin, I., 2005, Ice-sheet and sea-level changes. *Science* 310, 456-460.

Alvarez, W., Ammerman, A.J., Renne, P.R., Karner, D.B., Terrenato, N., Montanari, A., 1996. Quaternary fluvial-volcanic stratigraphy and geochronology of the Capitoline hill in Rome. *Geology* 24, 751-754.

Barker, S., Chen, J., Gong, X., Jonkers, L., Knorr, G., Thornalley, D., 2015. Icebergs not the trigger for North Atlantic cold events. *Nature* 7547, 333-336.

Barker, S., Diz, P., Vautravers, M.J., Pike, J., Knorr, G., Hall, I.R., Broecker, W.S., 2009. Interhemispheric Atlantic seesaw response during the last deglaciation. *Nature* 457, 1097-1102.

Barker, S., Knorr, G., Edwards, L., Parrenin, F., Putnam, A.E., Skinner, L.C., Wolff, E., Ziegler, M., 2011. 800,000 years of abrupt climate variability. *Science* 334, 347-351

[Blum, M.D., Toomey, R.S., Valastro, S., 1994. Fluvial response to Late Quaternary climatic and environmental change, Edwards Plateau, Texas. \*Palaeogeography, Palaeoclimatology, Palaeoecology\* 108, 1-21.](#)

Bond, G., Broecker, W., Johnsen, S., McManus, J., Labeyrie, L., Jouzel, J., Bonani, G., 1993. Correlations between climate records from North Atlantic sediments and Greenland ice. *Nature* 365, 143-147.

Bowen, D.Q., 2010. Sea level ~400 000 years ago (MIS 11): analogue for present and future sea-level? *Climate of Past* 6, 19-29.

Brendryen, J., Haflidason, H., Yokoyama, Y., Haaga, K. A., Hannisdal, B., 2020. Eurasian Ice Sheet collapse was a major source of Meltwater Pulse 1A 14,600 years ago. *Nature Geoscience* 13, 363-368.

Broecker, W. S., Bond, G., Klas, M., Clark E., McManus, J., 1992. Origin of the northern Atlantic's Heinrich events. *Climate Dynamics*. 6, 265– 273, doi:10.1007/BF00193540.

Chappell, J., 2002. Sea level changes forced ice breakouts in the Last Glacial cycle: new results from coral terraces. *Quaternary Science Reviews* 21, 1229-1240.

Chappell, J., Shackleton, N., 1986. Oxygen isotopes and sea level. *Nature*, 324(6093), 137-140.

Cheng, H., Edwards, R.L., Broecker, W.S., Denton, G.H., Kong, X. Wang, Y, Zhang, R., Wang, X., 2009. Ice Age Terminations. *Science* 326, 248-252. DOI:10.1126/science.1177840

Clark, P.U., Dyke, A.S., Shakun, J.D., Carlson, A.E., Clark, J., Wohlfarth, B., Mitrovica, J.X., Hostetler, S.W, McCabe, A.M., 2009. The Last Glacial Maximum. *Science* 325, 710-714.



1 Clement, A.C., and Peterson L.C., 2008), Mechanisms of abrupt climate change of the last glacial period, *Rev.*  
2 *Geophys.*, 46, RG4002, doi:10.1029/2006RG000204

3 Conato, V., Esu, D., Malatesta, A., Zarlenga, F., 1980. New data on the Pleistocene of Rome. *Quaternaria* 22,  
4 131–176.

5 Conticelli, S., Peccerillo, A., 1992. Petrology and geochemistry of potassic and ultrapotassic volcanism in  
6 Central Italy: petrogenesis and inferences on the evolution of the mantle sources. *Lithos* 28, 221-240.

7 Deschamps, P., Durand, N., Bard, E., Hamelin, B., Camoin, G., Thomas, A.L., Henderson, G.M., Okuno, J,  
8 Yokoyama, Y., 2012. Ice-sheet collapse and sea-level rise at the Bølling warming 14,600 years ago. *Nature*  
9 483, 559-564.

10 Dutton, A, Lambeck, K., 2012. Ice volume and sea level during the last interglacial. *Science* 337, 216–219.

11 Dutton, A., Carlson, A.E., Long, A.J., Milne, G.A., Clark, P.U., DeConto, R., Horton, B.P., Rahmstorf, S.,  
12 Raymo, M.E., 2015. Sea-level rise due to polar ice-sheet mass loss during past warm periods. *Science* 349,  
13 aaa4019.

14 Fairbanks, R.G., 1989. A 17,000-year glacio-eustatic sea level record: influence of glacial melting rates on the  
15 Younger Dryas event and deep-ocean circulation. *Nature* 342, 637-642.

16 Ferranti, L., Antonioli, F., Mauze, B., Amorosi, A., Dai Pra, G., Mastronuzzi, G., Monaco, C., Orrù, P.,  
17 Pappalardo, M., Radtke, U., Renda, P., Romano, P., Sansò, P., Verrubbi, V., 2006. Markers of the last  
18 interglacial sea-level high stand along the coast of Italy: Tectonic implications. *Quaternary International*  
19 145/146, 30-54.

20 Florindo, F., Karner, D.B., Marra, F., Renne, P.R., Roberts A.P., Weaver, R., 2007. Radioisotopic age  
21 constraints for Glacial Terminations IX and VII from aggradational sections of the Tiber River delta in  
22 Rome, Italy. *Earth and Planetary Science Letters* 256, 61-80. doi: 10.1016/j.epsl.2007.01.014.

23 Giaccio, B., Leicher, N., Mannella, G., Monaco, L., Regattieri, E., Wagner, B., Zanchetta, G., Gaeta, M., Marra,  
24 F. Nomade, S., Palladino, D.M., Pereira, A., Scheidt, S., Sottili, G., Wonik, T., Wulf, S., Zeeden, C.,  
25 Ariztegui, D., Cavinato, G.P., Dean, J. Florindo, F., Leng, M., Macri, P., Niespolo, E., Renne, P.R., Rolf, C.,  
26 Sadori, L., Thomas, C., Tzedakis, C., 2019. Extending the tephra and palaeoenvironmental record of the  
27 Central Mediterranean back to 430 ka: A new core from Fucino Basin, central Italy. *Quaternary Science*  
28 *Reviews* 225: 106003.

29 Giraudi, C., Frezzotti, M., 1997. Late Pleistocene glacial events in the central Apennines, Italy. *Quaternary*  
30 *Research*, 48, 280-290.

1 Grant, K.M., Rohling, E.J., Ramsey, C.B., Cheng, H., Edwards, R.L., Florindo, F., Heslop, D., Marra, F.,  
2 Roberts, A.P., Tamisiea, M.E., Williams, F., 2014. Sea-level variability over five glacial cycles. *Nature*  
3 *Communications* 5, 5076. doi:10.1038/ncomms6076

4 Hansen, J., Sato, M., Russell, G., Kharecha, P., 2013. Climate sensitivity, sea level and atmospheric carbon  
5 dioxide. *Philosophical Transactions of the Royal Society A: Mathematical, Physical and Engineering*  
6 *Sciences* 371, 20120294.

7 Hays, J.D., Imbrie, J., Shackleton, N.J., 1976. Variations in the Earth's orbit: pacemaker of the ice  
8 ages. *Science* 194, 1121-1132.

9 Hemming, S. R., 2004. Heinrich events: Massive late Pleistocene detritus layers of the North Atlantic and their  
10 global climate imprint. *Reviews of Geophysics* 42, RG1005. doi:10.1029/2003RG000128.

11 Jouzel, J., Masson-Delmotte, V., Cattani, O., Dreyfus, G., Falourd, S., Hoffmann, G., Minster, B., Nouet, J.,  
12 Barnola, J.M., Chappellaz, J., Fischer, H., Gallet, J.C., Johnsen, S., Leuenberger, M., Loulergue, L., Luethi,  
13 D., Oerter, H., Parrenin, F., Raisbeck, G., Raynaud, D., Schilt, A., Schwander, J., Selmo, E., Souchez, R.,  
14 Spahni, R., Stauffer, B., Steffensen, J.P., Stenni, B., Stocker, T.F., Tison, J.L., Werner, M., Wolff, E.W.,  
15 2007. Orbital and millennial antarctic climate variability over the past 800,000 years. *Science* 317, 793-796.

16 Karner, D.B., Marra, F., 1998. Correlation of fluviodeltaic aggradational sections with glacial climate history: A  
17 revision of the Pleistocene stratigraphy of Rome. *Geological Society of America Bulletin* 110, 748-758.

18 Karner, D.B., Marra, F., 2003.  $^{40}\text{Ar}/^{39}\text{Ar}$  dating of Glacial Termination V and duration of the Stage 11  
19 highstand, in: Droxler, A.W., Poore, R.Z., Burckle, L.H. (Eds.), *Earth's Climate and Orbital Eccentricity: The*  
20 *Marine Isotope Stage 11 Question*, American Geophysical Union, *Geophysical Monograph*, 137, 61-66.

21 Karner, D.B., Marra, F., Florindo, F., Boschi, E., 2001a. Pulsed uplift estimated from terrace elevations in the  
22 coast of Rome: Evidence for a new phase of volcanic activity? *Earth and Planetary Science Letters* 188, 135-  
23 148.

24 Karner, D.B., Marra, F., Renne, P.R., 2001b. The history of the Monti Sabatini and Alban Hills volcanoes:  
25 groundwork for assessing volcanic-tectonic hazards for Rome. *Journal of Volcanology and Geothermal*  
26 *Research*, 107, 185-219.

27 Karner, D.B., Renne, P.R., 1998.  $^{40}\text{Ar}/^{39}\text{Ar}$  geochronology of Roman volcanic province tephra in the Tiber  
28 River valley: Age calibration of middle Pleistocene sea-level changes. *Geological Society of America*  
29 *Bulletin* 110, 740-747.

30 Knutti, R., Flückiger, J., Stocker, T. F., Timmermann, A., 2004. Strong hemispheric coupling of glacial climate  
31 through freshwater discharge and ocean circulation. *Nature* 430, 851-856.

1 Köhler P, Bintanja R, Fischer H, Joos F, Knutti R, Lohmann, G., Masson-Delmotte, V., 2010. What caused  
2 Earth's temperature variations during the last 800,000 years? Data-based evidence on radiative forcing and  
3 constraints on climate sensitivity. *Quaternary Science Reviews* 29, 129-45.

4 Jansen, J. H. F., Kuijpers, A. & Troelstra, S. R. A. Mid-Brunhes climatic event: long-term changes in global  
5 atmosphere and ocean circulation. *Science* 232, 619–622 (1986)

6 Lambeck, K., Rouby, H., Purcell, A., Sun, Y., Sambridge, M., 2014. Sea level and global ice volumes from the  
7 Last Glacial Maximum to the Holocene. *Proceedings of the National Academy of Sciences* 111, 15296-  
8 15303.

9 Laskar, J., Robutel, P., Joutel, F., Gastineau, M., Correia, A. C. M., Levrard, B., 2004. A long-term numerical  
10 solution for the insolation quantities of the Earth. *Astronomy & Astrophysics* 428, 261-285.

11 Luberti, G.M., Marra, F., Florindo, F., 2017. A review of the stratigraphy of Rome (Italy) according to  
12 geochronologically and paleomagnetically constrained aggradational successions, glacio-eustatic forcing and  
13 volcano-tectonic processes. *Quaternary International*, 438, 40-67.  
14 <http://dx.doi.org/10.1016/j.quaint.2017.01.044>

15 Malinverno, A., Ryan, W.B.F., 1986. Extension in the Tyrrhenian sea and shortening in the Apennines as results  
16 of arc migration driven by sinking of the lithosphere. *Tectonics* 5, 227-245.

17 Marino, G., Rohling, E.J., Rodríguez-Sanz, L., Grant, K.M., Heslop, D., Roberts, A.P., Stanford, J.D, Yu, J.,  
18 2015. Bipolar seesaw control on last interglacial sea level. *Nature* 522, 197-201.

19 Marra, F., Rosa, C., 1995. Stratigrafia e assetto geologico dell'area romana. In: Funicello, R. (Ed.), *La Geologia*  
20 *di Roma*". Mem. Des. d. Carta Geol. d'It., 50, pp. 49–118.

21 Marra, F., Florindo, F., 2014. The subsurface geology of Rome: Sedimentary processes, sea-level changes and  
22 astronomical forcing. *Earth-Science Reviews* 136, 1-20.

23 Marra, F., Florindo, F., Boschi, E., 2008. History of glacial terminations from the Tiber River, Rome: Insights  
24 into glacial forcing mechanisms. *Paleoceanography* 23, 1-17. doi:10.1029/2007PA001543

25 Marra F., D.B. Karner, C. Freda, M. Gaeta, P.R. Renne (2009) - Large mafic eruptions at the Alban Hills  
26 Volcanic District (Central Italy): chronostratigraphy, petrography and eruptive behavior, *Journal of*  
27 *Volcanology and Geothermal Research* 179, 217-232 doi:10.1016/j.jvolgeores.2008.11.009

28 Marra F., Sottili, G., Gaeta, M., Giaccio, B., Jicha, B., Masotta, M., Palladino, D.M., Deocampo, D., 2014.  
29 Major explosive activity in the Sabatini Volcanic District (central Italy) over the 800-390 ka interval:  
30 geochronological - geochemical overview and tephrostratigraphic implications, *Quaternary Science Reviews*,  
31 94, 74-101. doi:10.1016/j.quascirev.2014.04.010

1 Marra, F., Rohling, E.J., Florindo, F., Jicha, B., Nomade, S., Pereira, A., Renne, P.R., 2016a. Independent  
2  $^{40}\text{Ar}/^{39}\text{Ar}$  and  $^{14}\text{C}$  age constraints on the last five glacial terminations from the aggradational successions of  
3 the Tiber River, Rome (Italy). *Earth Planet Sci. Lett.* 449, 105-117. doi:10.1016/j.epsl.2016.05.037

4 Marra, F., Florindo, F., Anzidei, M., & Sepe, V., 2016b. Paleo-surfaces of glacio-eustatically forced  
5 aggradational successions in the coastal area of Rome: assessing interplay between tectonics and sea-level  
6 during the last ten interglacials. *Quaternary Science Reviews* 148, 85-100.  
7 <http://dx.doi.org/10.1016/j.quascirev.2016.07.003>

8 Marra, F., Jicha, B., Florindo, F., 2017.  $^{40}\text{Ar}/^{39}\text{Ar}$  dating of Glacial Termination VI: constraints to the duration  
9 of Marine Isotopic Stage 13. *Scientific Reports* 7, 8908. doi:10.1038/s41598-017-08614-6

10 Marra, F. Gaeta, M. Jicha, B.R. Nicosia, C. Tolomei, C. Ceruleo, P. Florindo, F. Gatta, M. La Rosa, M. Rolfo,  
11 M.F., 2019a. MIS 9 to MIS 5 terraces along the Tyrrhenian Sea coast of Latium (central Italy): assessing  
12 interplay between sea-level oscillations and tectonic movements, *Geomorphology* 346: 106843.  
13 DOI:10.1016/j.geomorph.2019.106843

14 Marra, F. Costantini, L., Di Buduo, G.M. Florindo, F., Jicha, B.R., Monaco, L., Palladino, D.M., Sottili, G.,  
15 2019b. Combined glacio-eustatic forcing and volcano-tectonic uplift: geomorphological and  
16 geochronological constraints on the Tiber River terraces in the eastern Vulsini Volcanic District (central  
17 Italy). *Global and Planetary Change* 182,103009. doi:10.1016/j.gloplacha.2019.103009.

18 Marra, F., Castellano, C., Cucci, L., Florindo, F., Gaeta, M., Jicha, B., Palladino, D.M., Sottili, G., Tertulliani, A.,  
19 Tolomei, C., 2020. Monti Sabatini and Colli Albani: the dormant twin volcanoes at the gates of Rome,  
20 *Scientific Reports* 10(1), 8666.

21 Martínez-Botí, M.A., Foster, G.L., Chalk, T.B., Rohling, E.J., Sexton, P.F., Lunt, D.J., Pancost, R.D., Badger,  
22 M.P.S., Schmidt, D.N., 2015. Plio-Pleistocene climate sensitivity evaluated using high-resolution  $\text{CO}_2$   
23 records. *Nature* 518, 49-54.

24 Milankovitch, M.R., 1941. *Serb. Acad. Special Publ.* 132, Belgrade (1941).

25 Milli, S., 1997. Depositional setting and high-frequency sequence stratigraphy of the Middle-Upper Pleistocene  
26 to Holocene deposits of the Roman Basin. *Geol. Romana* 33, 99–136.

27 Milli, S., Moscatelli, M., Palombo, M.R., Parlagreco, L., Paciucci, M., 2008. Incised valleys, their filling and  
28 mammal fossil record - A case study from Middle-Upper Pleistocene deposits of the Roman Basin (Latium,  
29 Italy). In: Amorosi, A., Haq, B.U., Sabato, L. (Eds.), *Advances in Application of Sequence Stratigraphy in*  
30 *Italy. GeoActa (Special Publication)*, 1, pp. 667–687.

31

1 Niespolo, E. M., Rutte, D., Deino, A. L., Renne, P. R., 2017. Intercalibration and age of the Alder Creek sanidine  
2  $^{40}\text{Ar}/^{39}\text{Ar}$  standard. *Quaternary Geochronology*, 39, 205-213. Nomade, S., Gauthier, A., Guillou, H., Pastre,  
3 J.F., 2010.  $^{40}\text{Ar}/^{39}\text{Ar}$  temporal framework for the Alleret maar lacustrine sequence (French Massif-Central):  
4 Volcanological and paleoclimatic implications. *Quaternary Geochronology* 5, 20-27.

5 North Greenland Ice Core Project Members, 2004. High-resolution record of Northern Hemisphere climate  
6 extending into the last interglacial period. *Nature* 431, 147-151.

7 Patacca, E., Sartori, R., Scandone, P., 1990. Tyrrhenian basin and apenninic arcs: kinematic relations since late  
8 Tortonian times. *Memorie della Società Geologica Italiana* 45, 425-451.

9 Pereira, A., Monaco, L., Marra, F., Nomade, S., Gaeta, M., Leicher, N., Palladino, D.M., Sottili, G., Guillou, H.,  
10 Scao, V., Giaccio, B., 2020. Tephrochronology of the central Mediterranean MIS 11c interglacial (~425-395  
11 ka): new constraints from Vico volcano and Tiber delta, Central Italy. *Quaternary Science Reviews* 243:  
12 106470.

13 Rahmstorf, S., 2002. Ocean circulation and climate during the past 120,000 years. *Nature* 419, 207-214.

14 Railsback, L.B., Gibbard, P.L., Head, M.J., Voarintsoa, N.R.G., Toucanne, S., 2015. An optimized scheme of  
15 lettered marine isotope substages for the last 1.0 million years, and the climatostratigraphic nature of isotope  
16 stages and substages. *Quaternary Science Reviews*, 111, 94-106.

17 Raymo, M., Mitrovica, J. Collapse of polar ice sheets during the stage 11 interglacial. *Nature* 483, 453–456  
18 (2012). <https://doi.org/10.1038/nature10891>

19 Renne, P.R., Mundil, R., Balco, G., Min, K., Ludwig, K.R. 2010. Joint determination of  $^{40}\text{K}$  decay constants and  
20  $^{40}\text{Ar}^*/^{40}\text{K}$  for the Fish Canyon sanidine standard, and improved accuracy for  $^{40}\text{Ar}/^{39}\text{Ar}$  geochronology.  
21 *Geochimica Cosmochimica Acta* 74, 5349-5367.

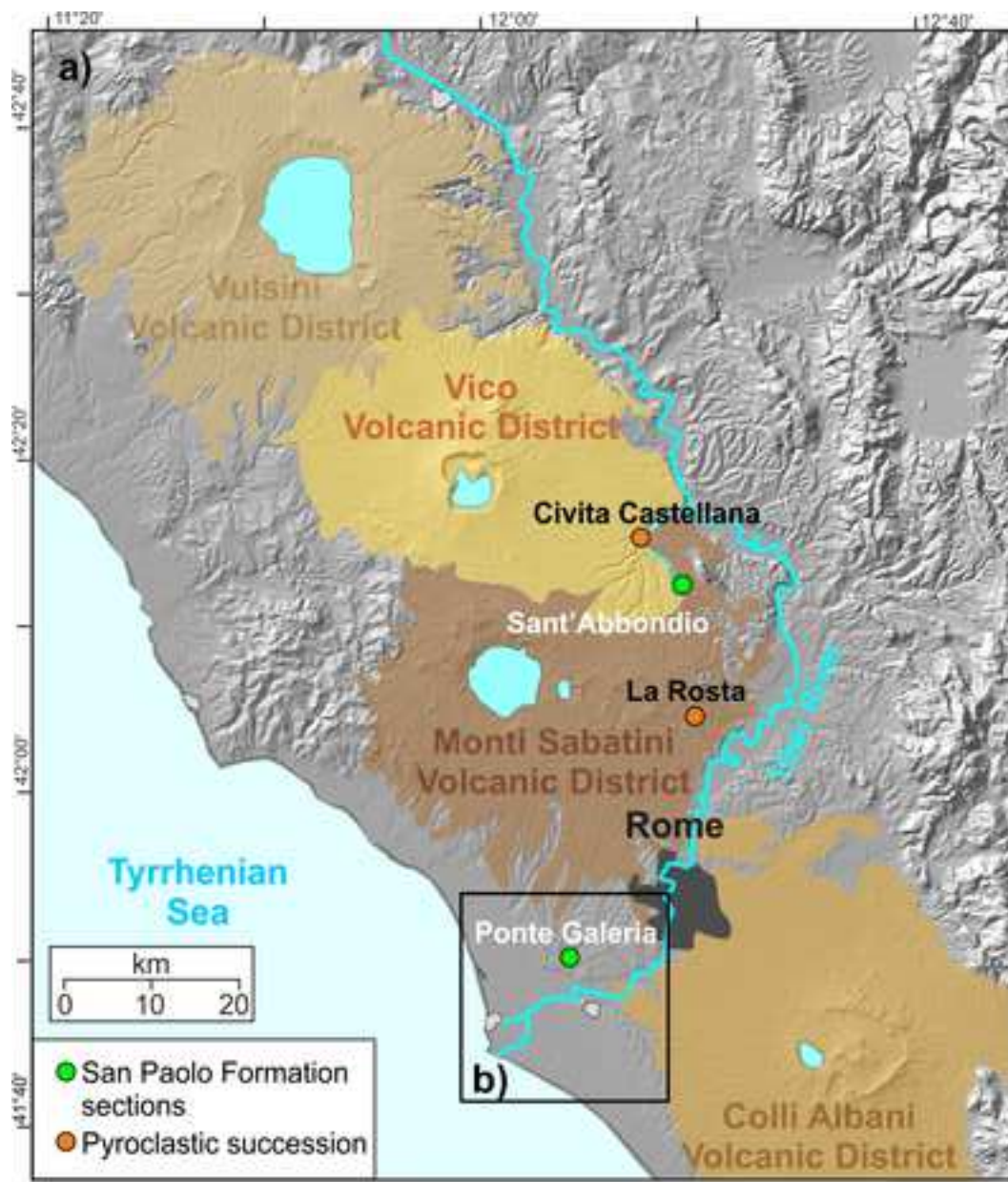
22 Renne, P.R., Mundil, L.R., Balco, G., Min, K. et Ludwig, K.R., 2011. Joint determination of  $^{40}\text{K}$  decay  
23 constants and  $^{40}\text{Ar}^*/^{40}\text{K}$  for the Fish Canyon sanidine standard, and improved accuracy for  $^{40}\text{Ar}/^{39}\text{Ar}$   
24 geochronology. Response to the comment by W.H. Schwarz et al. *Geochimica Cosmochimica Acta* 75, 5097-  
25 5100.

26 Rodrigues, T., Voelker, A. H. L., Grimalt, J. O., Abrantes, F., Naughton, F., 2011. Iberian Margin sea surface  
27 temperature during MIS 15 to 9 (580–300 ka): Glacial suborbital variability versus interglacial  
28 stability. *Paleoceanography* 26, PA1204.

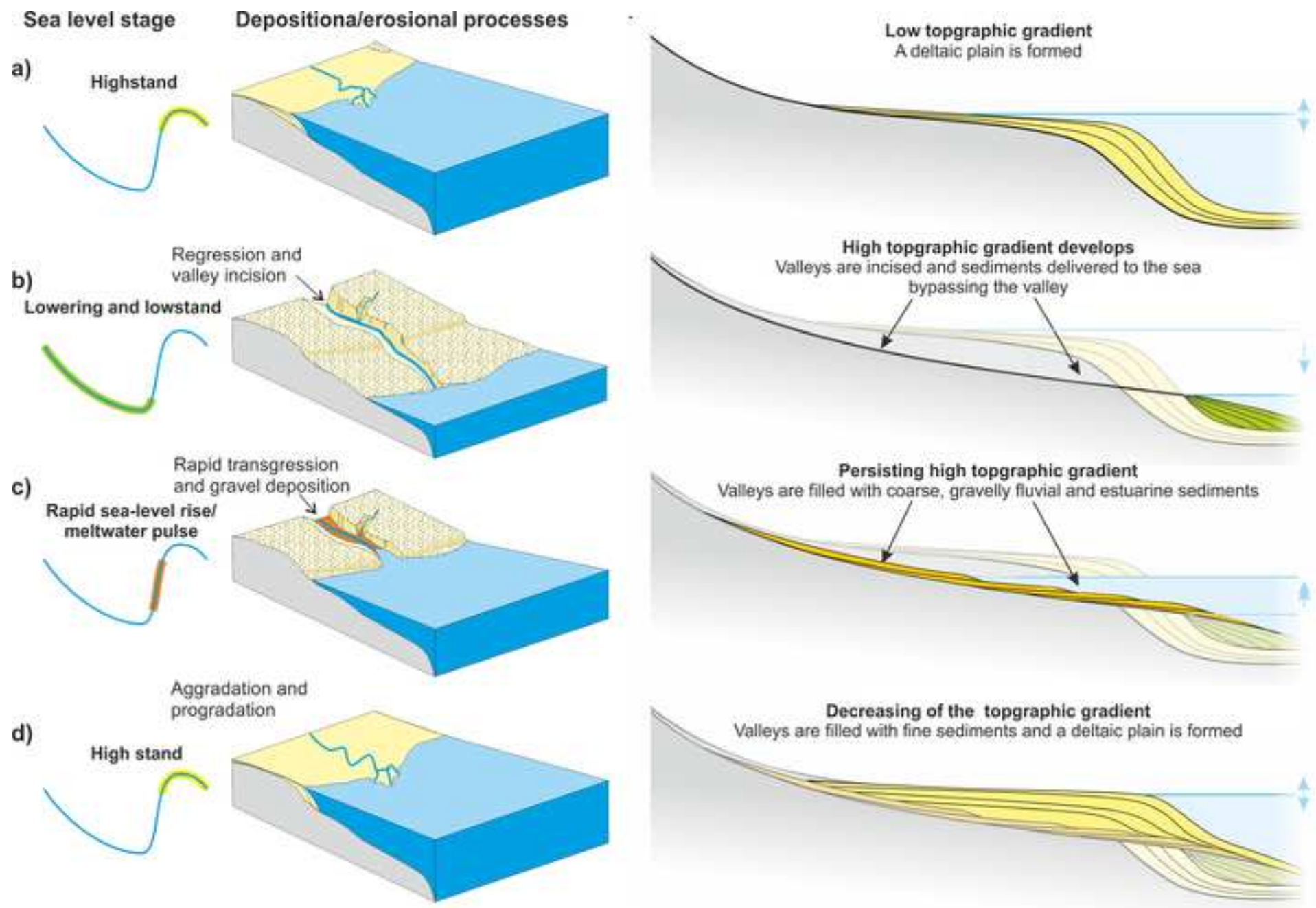
29 Rohling, E.J, Medina-Elizalde M, Shepherd, J.G., Siddall, M., Stanford, J.D., 2012. Sea surface and high-  
30 latitude temperature sensitivity to radiative forcing of climate over several glacial cycles. *Journal of Climate*  
31 25, 1635-1656.

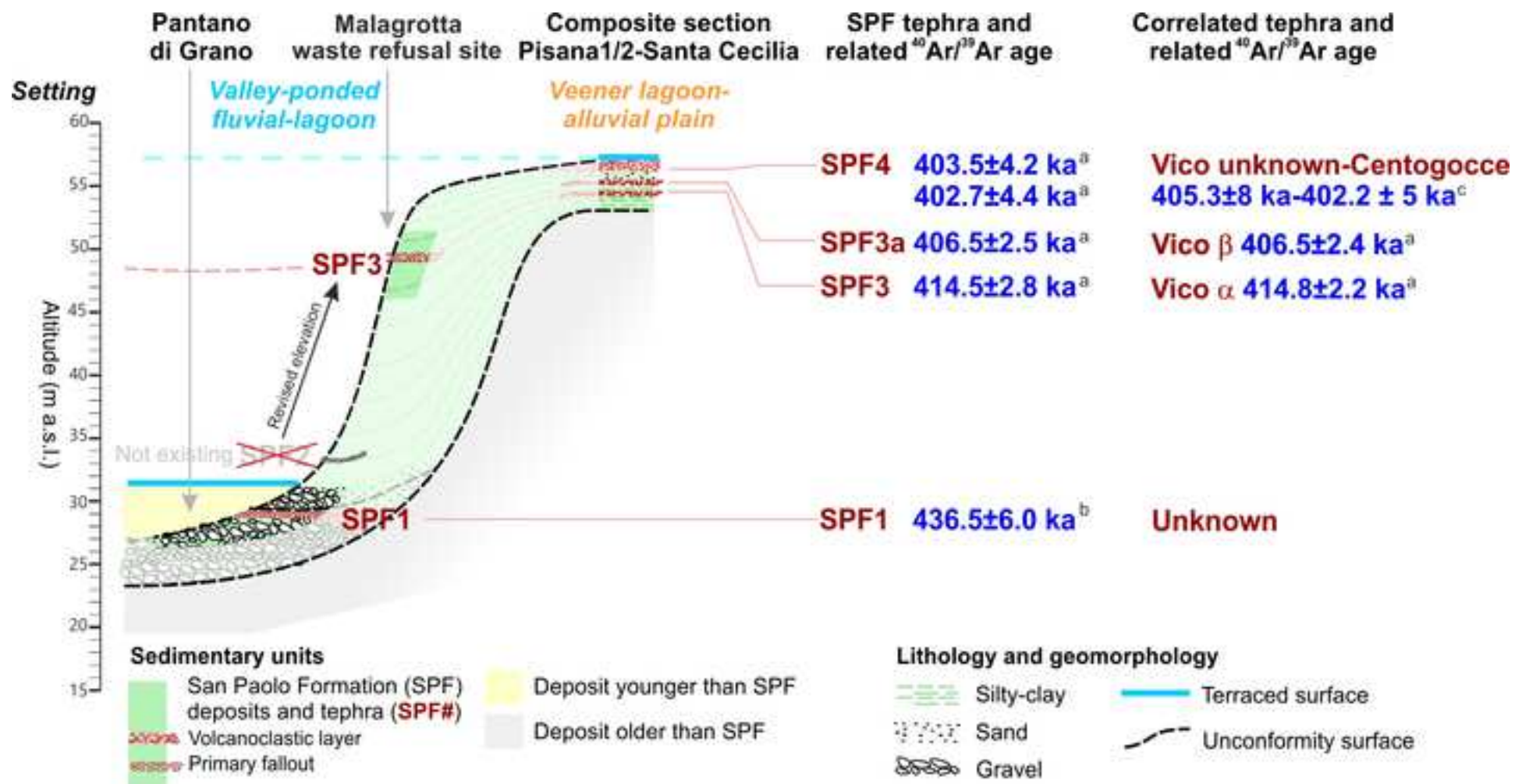
- 1 Rohling, E.J., Foster, G.L., Grant, K.M., Marino, G., Roberts, A.P., Tamisiea, M.E, Williams, F., 2014. Sea-  
2 level and deep-sea-temperature variability over the past 5.3 million years. *Nature* 508, 477-482.
- 3 Rohling, E.J., Grant, K., Bolshaw, M., Roberts, A.P., Siddall, M., Hemleben, C, Kucera, M., 2009. Antarctic  
4 temperature and global sea level closely coupled over the past five glacial cycles. *Nature Geoscience* 2, 500-  
5 504.
- 6 Rohling, E.J., Hibbert, F.D., Williams, F.H., Grant, K.M., Marino, G., Foster, G.L., Hennekam, R., de Lange,  
7 G.J., Roberts, A.P., Yu, J., Webster, J.M, Yokoyama, Y., 2017. Differences between the last two glacial  
8 maxima and implications for ice-sheet,  $\delta^{18}O$ , and sea-level reconstructions. *Quaternary Science Reviews*  
9 176, 1-28.
- 10 Rohling, E.J., Marino, G., Foster, G.L., Goodwin, P.A., von der Heydt, A.S., Köhler, P., 2018. Comparing  
11 Climate Sensitivity. Past and Present. *Annual Review of Marine Science* 10, 261-288.
- 12 Rohling, E.J., Marsh, R., Wells, N.C., Siddall, M, Edwards, N.R., 2004. Similar meltwater contributions to  
13 glacial sea level changes from Antarctic and northern ice sheets. *Nature* 430, 1016-1021.
- 14 Shackleton, N. J., 1969. The last interglacial in the marine and terrestrial records. *Proceedings of the Royal*  
15 *Society of London. Series B. Biological Sciences* 174, 135-154.
- 16 Shackleton, N. J., 2000. The 100,000-year ice-age cycle identified and found to lag temperature, carbon dioxide,  
17 and orbital eccentricity. *Science* 289, 1897-1902.
- 18 Siddall, M., Rohling, E.J., Almogi-Labin, A., Hemleben, C., Meischner, D., Schmelzer, I, Smeed, D.A., 2003.  
19 Sea-level fluctuations during the last glacial cycle. *Nature* 423, 853-858.
- 20 Snyder, C.W., 2016. Evolution of global temperature over the past two million years. *Nature* 538, 226-228.
- 21 Snoeckx, H., Grousset, F., Revel, M., Boelaert, A., 1999. European contribution of ice-rafted sand to Heinrich  
22 layers H3 and H4. *Marine Geology* 158, 197–208. doi:10.1016/S0025- 3227(98)00168- 6.
- 23 Sottili, G., Palladino, D.M., Marra, F., Jicha, B., Karner, D.B., Renne, P.R., 2010. Geochronology of the most  
24 recent activity in the Sabatini Volcanic District, Roman Province, central Italy. *Journal of Volcanology and*  
25 *Geothermal Research* 196, 20-30. doi:10.1016/j.jvolgeores.2010.07.003.
- 26 Stanford, J.D., Hemingway, R., Rohling, E.J., Challenor, P.G., Medina-Elizalde, M., Lester, A.J., 2011. Sea-  
27 level probability for the last deglaciation: a statistical analysis of far-field records. *Global and Planetary*  
28 *Change* 79, 193-203. <http://dx.doi.org/10.1016/j.gloplacha.2010.11.002>.
- 29 Thompson, W.G, Goldstein, S.L., 2005. Open-system coral ages reveal persistent suborbital sea-level cycles.  
30 *Science* 308, 401-404.

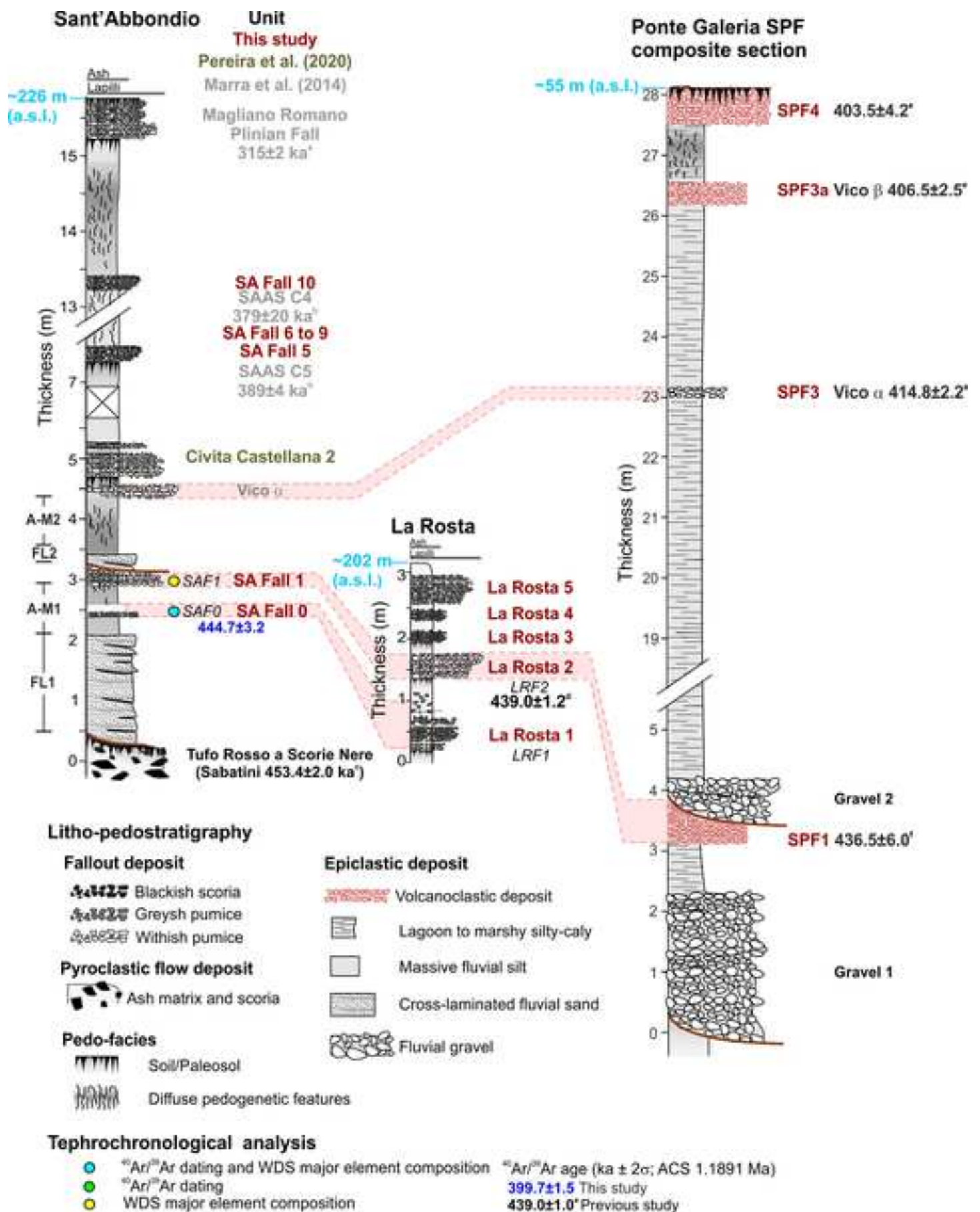
- 1 Tzedakis, P.C., Channell, J.E.T., Hodell, D.A., Kleiven, H.F, Skinner, L.C., 2012. Determining the natural length  
2 of the current interglacial. *Nature Geoscience* 5, 138-142.
- 3 Tzedakis, P.C., Crucifix, M., Mitsui, T, Wolff, E.W., 2017. A simple rule to determine which insolation cycles  
4 lead to interglacials. *Nature* 542, 427-432.
- 5 Villa, P., Soriano, S., Grün, R., Marra, F., Nomade, S., Pereira, A., Boschian, G., Pollarolo, L., Fang, F., Bahain,  
6 J.J., 2016. The Acheulian and early Middle Paleolithic in Central Italy: Stability and Innovation. *PLoS ONE*  
7 11, e0160516. doi:10.1371/journal.pone.0160516.
- 8 Yokoyama, Y., Esat, T.M., Thompson, W.G., Thomas, A.L., Webster, J.M., Miyairi, Y., Sawada, C., Aze, T.,  
9 Matsuzaki, H., Okuno, J., Fallon, S., Braga, J.-., Humblet, M., Iryu, Y., Potts, D.C., Fujita, K., Suzuki, A.,  
10 Kan, H., 2018. Rapid glaciation and a two-step sea level plunge into the Last Glacial Maximum. *Nature* 559,  
11 603-607.
- 12

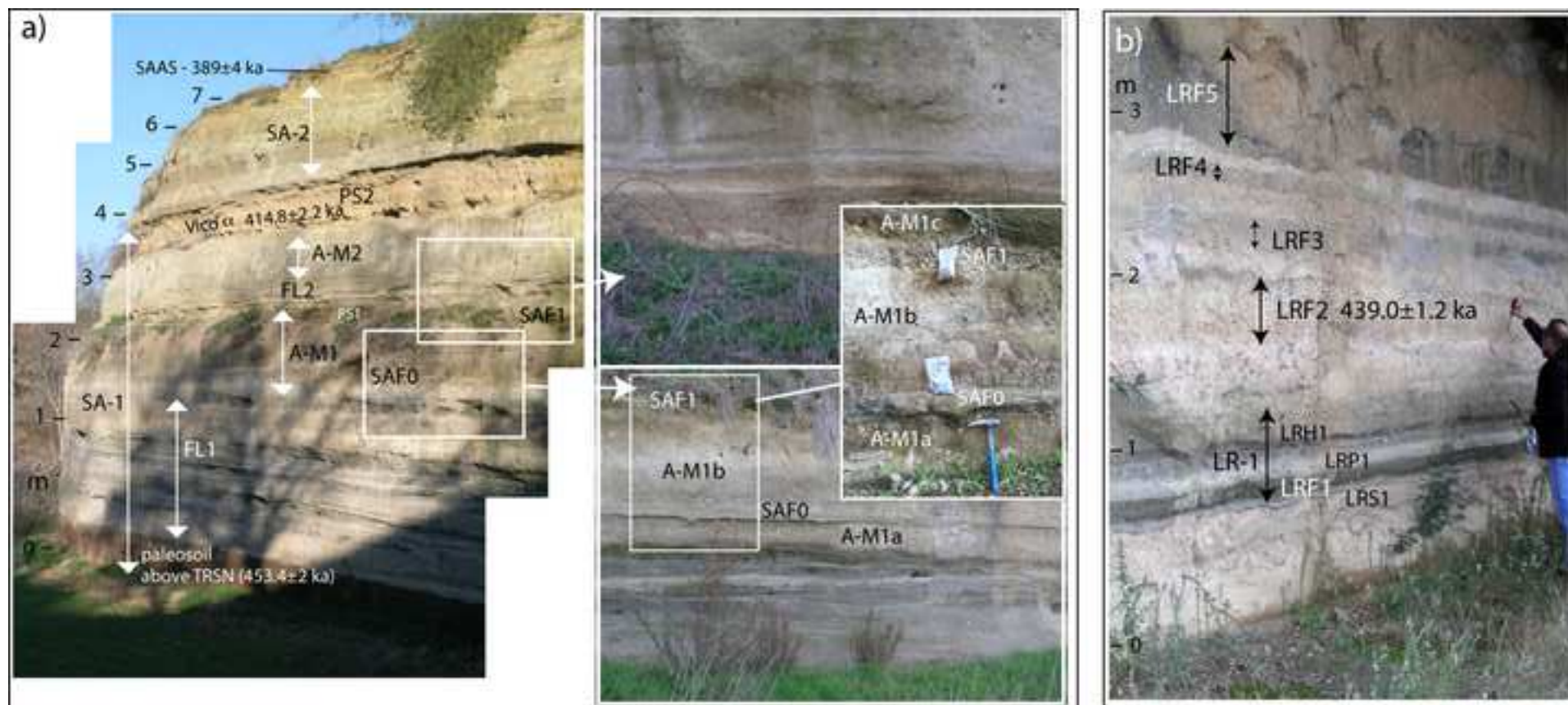


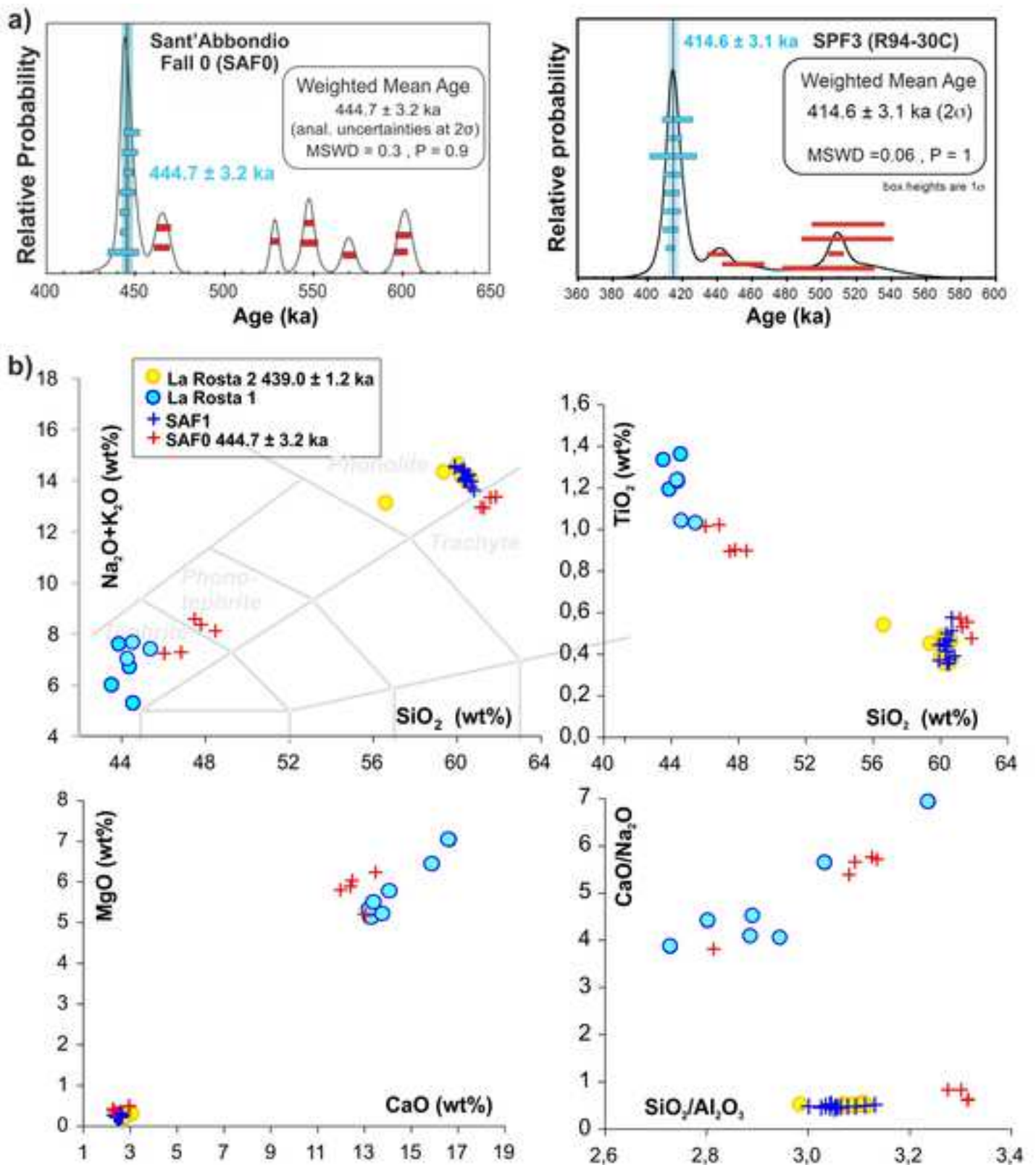




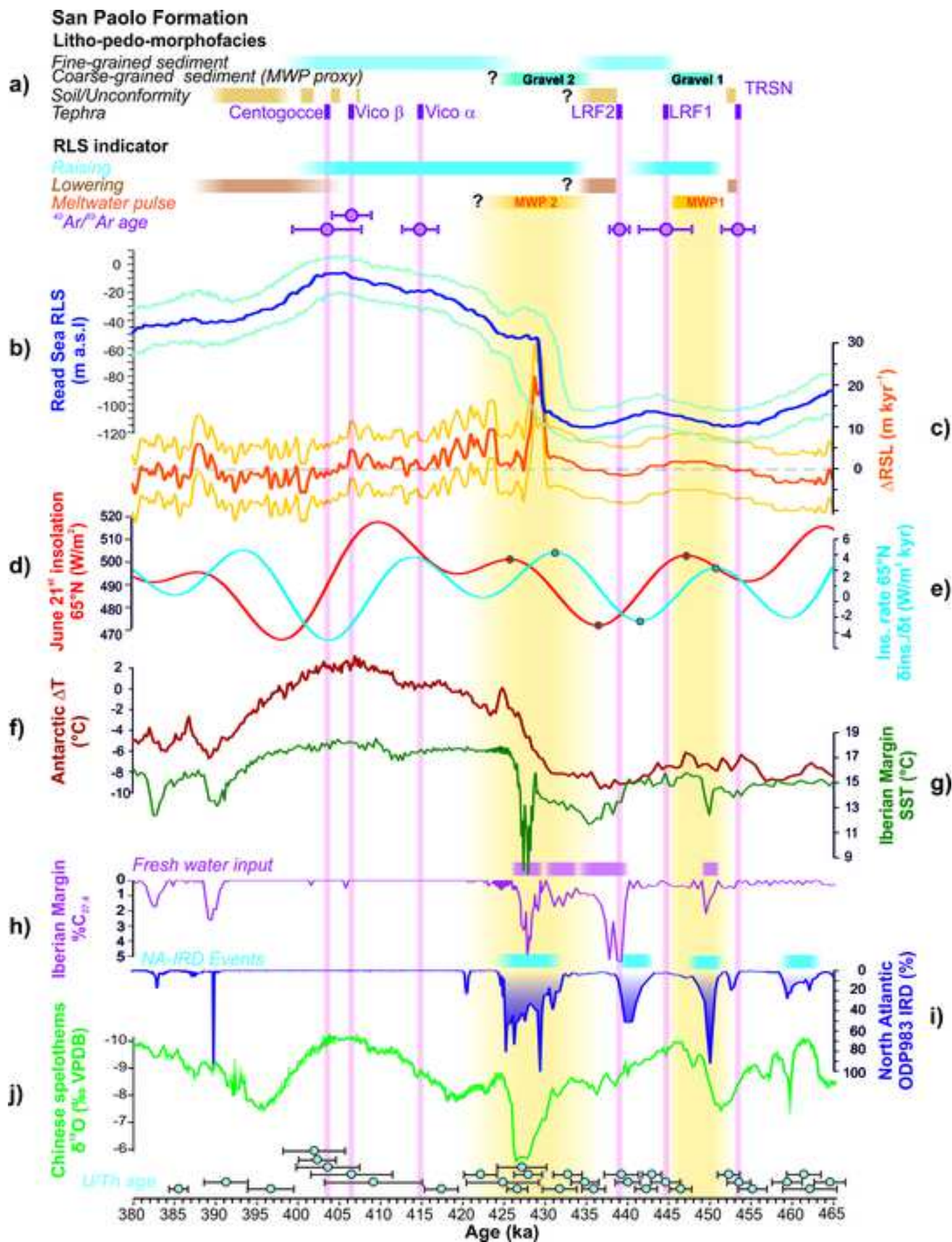












### Declaration of interests

The authors declare that they have no known competing financial interests or personal relationships that could have appeared to influence the work reported in this paper.

The authors declare the following financial interests/personal relationships which may be considered as potential competing interests:

On behalf all of the authors,  
Fabrizio Marra





## AUTHOR'S CONTRIBUTION

**BG:** Conceptualization, Validation, Investigation, Writing - Original Draft, Visualization  
**GM:** Conceptualization, Validation, Writing - Original Draft, Visualization  
**FM:** Conceptualization, Methodology, Validation, Investigation, Writing - Original Draft, Visualization  
**LM:** Investigation, Validation, Data Curation, Writing - Review & Editing  
**AP:** Investigation, Methodology, Validation, Data Curation, Writing - Review & Editing  
**GZ:** Validation, Writing - Review & Editing  
**MG:** Data Curation, Validation, Writing - Review & Editing  
**NL:** Data Curation, Validation, Writing - Review & Editing  
**SN:** Investigation, Methodology, Validation, Data Curation, Writing - Review & Editing  
**DMP:** Investigation, Validation, Writing - Review & Editing  
**GS:** Investigation, Validation, Writing - Review & Editing  
**HG:** Methodology, Validation, Data Curation  
**VS:** Methodology, Validation, Data Curation



Click here to access/download

**e-Component/Supplementary data**

Supplementary dataset 1\_Ar\_Ar data.xlsx





Click here to access/download

**e-Component/Supplementary data**  
Supplementary dataset 2\_WDS glass  
composition\_rev.xlsx